Microscopic and Macroscopic Samples of Atoms in Superposition States Studied by Attosecond Pulses

Axel Stenquist

Thesis submitted for the degree of Master of Science
Project duration: 12 months

Supervised by
Felipe Zapata Abellán and Jan Marcus Dahlström

LUNDS UNIVERSITET

Department of Physics
Division of Mathematical Physics
May 2021

Abstract

In the present thesis, the interaction between atoms in superposition states and attosecond pulses is studied from the microscopic to the macroscopic regime. Using a semi-classical framework, three different models have been explored in order to investigate attosecond light–matter interaction processes.

The first model is a microscopic, single-atom model. Through using this model, the absorption and the radiation of an external attosecond pulse was studied for several atomic superposition states and pulse energies. The second model was composed by two coupled atoms, where the interaction was described by either dipole-dipole or radiation interaction. The model was validated by simulating the Förster resonant phenomena. In addition, this model was used to determine the behaviour of the interactions with respect to separation distance and the initial states of the atoms. It was found that dipole-dipole interaction is dominant in the near field, whilst radiation interaction is dominant in the far field. Additionally, it was found that superpositions with high principal quantum numbers increase the strength of the dipole-dipole interaction but not the radiation interaction. The simulated results have been validated, in the short-time regime, using perturbation theory.

The last model investigated in this thesis is a macroscopic many-atom model. It was implemented in order to simulate the propagation of an attosecond pulse through a large sample of atoms. Utilising this model, collective effects of many-atom systems were studied. It was found that a macroscopic sample emits collimated radiation and that dissipation of pulse energy in a macroscopic sample retains the behaviour of radiation produced by a single atom but that it is deformed by the propagation through the sample.

The models explored in this thesis can be used in the study of light-matter interaction on the attosecond timescale with inter-atomic interactions and collective effects. The work presented here can be built on further to investigate research areas such as the dipole-blockade effect in cold atom physics, ionisation due to inter-atomic interaction or collective coherent effects.

List of Abbreviations

ATAS	Attosecond Transient Absorption Spectroscopy
CIS	Configuration-Interaction Singles
ECS	Exterior Complex Scaling
HHG	High-order Harmonic Generation
LG	Length Gauge
SOD	Second-Order Finite Differencing Scheme
TDSE	Time-Dependent Schrödinger Equation
TDCIS	Time-Dependent Configuration-Interaction Singles
VG	Velocity Gauge

Contents

1 Introduction **1**

2 Theory **3**
2.1 Microscopic Response . . . 3
2.1.1 Time-Dependent Hamiltonian and Wave Function . . . 3
2.1.2 Observables: Position, Velocity and Acceleration . . . 4
2.1.3 Attosecond Transient Absorption . . . 5
2.1.4 Radiation . . . 7
2.2 Macroscopic Response . . . 9
2.2.1 Two-Atom Model . . . 9
A Dipole-Dipole Interaction . . . 10
B Radiation Field Interaction . . . 11
2.2.2 Many-Atom One-Dimensional Model . . . 12
A Field Propagation Through a Macroscopic Sample . . . 12
B Radiation Emitted by Excited Macroscopic Sample . . . 14
C Energy Dissipation of Field in a Macroscopic Sample . . . 14

3 Methodology **16**
3.1 Time-Dependent Configuration-Interaction Singles . . . 16
3.1.1 Hartree-Fock Method . . . 16
3.1.2 Time-Dependent Hamiltonian and Wave Functions . . . 18
3.1.3 Numerical Resolution of the Equations of Motion . . . 19
3.1.4 Gauge Dependence of the TDCIS Method . . . 19
3.2 Numerical Methods and Computational Details . . . 20
3.2.1 Single-Atom Model . . . 20
A Numerical Computations of the Operators . . . 21
B State Populations in TDCIS . . . 22
3.2.2 Two-Atom Model . . . 22
3.2.3 Many-Atom Model . . . 23

4 Results and Discussion **25**
4.1 Single-Atom Response . . . 25
4.1.1 Observables of Atom Interacting with Attosecond Pulse . . . 26
4.1.2 ATAS of Hydrogen Atom in a Superposition State . . . 27
4.1.3 Radiation Emitted by Probed Hydrogen Atom in Superposition . . . 30
4.2 Two-Atom Model . . . 32
4.2.1 Two Coupled Hydrogen Atoms . . . 33
4.2.2 Two Coupled Helium Atoms . . . 39
4.3 Many-Atom Model . . . 41
4.3.1 Field Propagation . . . 41
4.3.2 Radiation Emitted by a Macroscopic Sample . . . 43
4.3.3 Macroscopic Energy Spectra . . . 44

5 Conclusion and Outlook **46**

Appendices 48

A Derivation of Observable Operators 48

B Transition Matrix Elements 50

C Numerical Representations of the Transition Matrix Elements 51

1 Introduction

In the 1920s, methods for the time-resolution of quantum dynamics were developed for the investigation of chemical reactions resolved on millisecond time scales through optical measurements of the reactants at constant flow through tubes [1]. In the 1950s, microsecond resolution was achieved by M. Eigen through observing the change in equilibrium for a chemical substance under rapid change of temperature, pressure or electric field [2]. With the discovery of the laser in the 1960s, nanosecond and picosecond resolution became available [3]. In the mid 1980s, femtosecond lasers were created, making way for the field of femtochemistry. This was an important step as it is on this timescale the atoms in molecules move, thus allowing for atomic dynamics to be resolved in time. Pump–probe methods are used to investigate chemical dynamics, such as molecular dissociation and transitions between states in molecules [4]. In the early 2000s experiments on the attosecond timescale were made possible through utilising high-order harmonic generation (HHG), which provides time controlled generation of attosecond extreme ultravioletpulses from broad infrared pulses [5]. In 2010 Goulielmakis *et al* conducted the first attosecond transient absorption spectroscopy (ATAS) experiment using HHG to investigate the dynamics of the valence electrons in Krypton [6]. Briefly, ATAS is used to investigate the energy absorbed by a quantum system from an external field, resolved on the attosecond timescale. ATAS is a pump–probe method. In a typical scenario, the quantum dynamics of the system is triggered by a pump laser pulse and probed with an attosecond pulse. The measured quantity is the absorption of the probe pulse. The two pulses are separated by a delay that is controlled in order to study the evolution of the system over time. The dynamics of the system are also resolved over energy, resulting in an absorption spectra which is resolved over both frequency and time delay. A theoretical and experimental review of ATAS is given in [7] and [8], respectively. These types of attosecond investigations are interesting because they probe dynamics on the typical timescale of electron movement in atoms, molecules and solids. The techniques of attosecond physics can be utilised to explore light–matter interaction phenomena, using tools such as ATAS.

Light–matter interaction is a vast subject that encapsulates both microscopic and macroscopic phenomena. The response of a many-atom system is different from that of independent atoms due to collective coherent effects. This was first described theoretically in 1954 by R. H. Dicke [9]. More details about these quantum effects, known as superradiance, can be found in a review written by Gross and Haroche [10]. Many-atom dynamics can be described by the semi-classical model of light–matter interaction. In such a model, where spontaneous emission is neglected, the atoms are handled quantum mechanically by solving the time-dependent Schrödinger equation (TDSE) and the fields are described classically by solving Maxwell's equations. In this semi-classical picture, many-atom dynamics will naturally evolve, provided that the atoms are initiated in dipole allowed superposition states. Dipole-dipole interaction gives rise to energy transfer between atoms through the Förster resonance phenomena [11]. A review of dipole-dipole interaction in Rydberg atoms is found in [12]. At short distances this type of interaction is important as the energy transfer scales with distance as R^{-6}. On the contrary, at larger atomic distances, energy transfer can be mediated by the radiation field described by Larmor's formula, where energy transfer scales with distance as R^{-2}. These two apparently different phenomena, Förster and radiation energy transfer, are in fact the short-range and long-range cases of a single mechanism,

as has been shown through quantum electrodynamical theory [13].

In this master thesis, properties of atoms in electronic superposition states are studied through their interaction with attosecond pulses. This was explored from the microscopic to the macroscopic regime. Effects beyond single-atom physics are studied by considering inter-atomic dipole-dipole and radiation interaction. In many light–matter investigations atoms are approximated by two-level systems, in this work however the whole electronic spectra is simulated including both bound and continuum states. The rationale for this is that atoms will transition from bound states to the continuum and then back to bound states again when they exchange high-energy photons from attosecond pulses. The hydrogen atom is considered as well as many-electron atoms described within the time-dependent configuration-interaction singles (TDCIS) method [14].

The absorbed and radiated energy, of a single-atom interacting with an external field, is calculated through ATAS and Larmor's formula respectively. Delay-dependence is achieved through varying the phase of the initial superposition state. Inter-atomic interactions were investigated by constructing a two-atom model and propagation models. The two-atom model couples one atom in a superposition state with another atom in its ground state. This is done in order to verify the Förster energy resonance phenomena. Through varying the atomic separation and the initial states the behaviour of the dipole-dipole and radiation interactions is studied. Macroscopic light–matter propagation is investigated through the construction of a many-atom model. Propagation of attosecond pulses through large samples of atoms coupled via their generated fields is studied. This is done with the aim of investigating the collective effects of the macroscopic sample in the presence of an external field. Using the many-atom model, effects such as collective radiation and wave-packet phase-dependent energy dissipation in a macroscopic sample is studied.

Using these models, attosecond aspects of light–matter interactions can be studied from the microscopic to the macroscopic regime. This is important in order to distinguish single-atom response from many-atom response to external excitation on the typical timescale of electron movement. Investigated phenomena includes the behaviour of probed superposition states of different angular momenta, ultra-fast resolution of Förster-like dynamics between atoms and collective effects of a macroscopic sample, such as the propagation of the attosecond pulse and the angular distribution of the macroscopic radiation.

2 Theory

In this section the theory used in this master thesis is presented. In Section 2.1 the single-atom response to an external perturbation is described. The time-dependent wave function is obtained by setting up the TDSE with the time-dependent Hamiltonian. Through use of the wave function the observables of position, velocity and acceleration are determined. The observables are used to describe the absorption and radiation of the atom. A semi-classical approach is utilised in which the atom is handled quantum mechanically and the field is handled in a classical manner. In Section 2.2 the theoretical framework for conducting simulations of macroscopic response is described. Two models are presented. The first is a two-atom model in which the atoms are coupled by either dipole-dipole interaction or radiation field interaction. The second model is a macroscopic many-atom model in which an electric field is propagated through a one-dimensional sample. Throughout this master thesis all expressions are described in terms of atomic units.

2.1 Microscopic Response

In this subsection the microscopic response of a single atom is described. In Section 2.1.1 the wave function and the Hamiltonian of the atom is presented and the interaction with an external perturbation is modelled by utilising the dipole approximation. In Section 2.1.2 the calculation of the observables of the atom, computed from their respective operators, are presented. In Section 2.1.3 the attosecond transient absorption of energy by the atom is calculated using the observables. In Section 2.1.4 the theory describing the radiation produced by a moving point charge, such as an electron, is presented.

2.1.1 Time-Dependent Hamiltonian and Wave Function

The time-dependent wave function is obtained by solving the TDSE, given by

$$i\frac{d}{dt}\left|\Psi(t)\right\rangle = \hat{H}(t)\left|\Psi(t)\right\rangle. \tag{1}$$

The expressions in this section are based on the work presented in [15]. The computation of the time-dependent wave functions are conducted through the TDCIS method as described in Section 3.1.

The time-dependent Hamiltonian is defined as

$$\hat{H}(t) = \hat{H} + \hat{V}(t), \tag{2}$$

where $\hat{V}(t)$ is the time-dependent perturbation, one-body operator, (e.g. interaction with an external electric field) and $\hat{H}$ is the field-free Hamiltonian given by

$$\hat{H} = \sum_{j=1}^{N}\left(\frac{\hat{p}_j^2}{2} - \frac{Z}{r_j}\right) + \sum_{j>k}^{N}\frac{1}{|\vec{r}_j - \vec{r}_k|}, \tag{3}$$

where the first term describes the one-electron kinetic energy and the electron-nucleus interaction, and the second term describes the electron-electron Coulomb interaction.

Neglecting the interaction with the magnetic field and assuming that the electric field is only a function of time, i.e. by implementing the dipole approximation [16], the interaction with an electromagnetic field can be given in *length gauge* (LG) or in *velocity gauge* (VG). Throughout this work only linearly polarised laser fields directed along the z-axis are used. Thus, the field interaction operator is defined by

$$\hat{V}(t) = \begin{cases} \hat{z}E(t); & \text{for LG,} \\ \hat{p}_z A(t) + \dfrac{A^2(t)}{2}; & \text{for VG,} \end{cases} \tag{4}$$

where $E(t)$ and $A(t)$ are the electric field and the vector potential respectively. The electric field and vector potential are related through $E(t) = -\dot{A}(t)$ (where the dot denotes the derivative with respect to time). $\hat{z}$ is the z-component of the one-body operators of position, it is define as

$$\hat{z} = \sum_{i=j}^{N} z_j, \tag{5}$$

and $\hat{p}_z$ is the z-component of the canonical momentum, defined as

$$\hat{p}_z = \sum_{j=1}^{N} -i\nabla_j, \tag{6}$$

where ∇_j acts in electron j.

The external field is defined as a Gaussian pulse through the vector potential as

$$A(t) = A_0 \cos(\omega_0(t - t_0)) \exp\left\{ \frac{2\ln(2)(t - t_0)^2}{\tau_e^2} \right\}, \tag{7}$$

where A_0 is the amplitude, ω_0 central frequency, t_0 is the delay time and τ_e is the pulse duration expressed as the full width at half-maximum.

2.1.2 Observables: Position, Velocity and Acceleration

In the Schrödinger picture of quantum mechanics, the time-dependent wave functions are used to calculate the physical quantities; i.e. the observables. The observables are calculated as the expectation value of the corresponding operator for the time-dependent wave function. In this section the derivation of the operators of position, velocity and acceleration is presented. The observables are used to investigate the response of the system to an external perturbation.

In this work, the observables of interest are the position, the velocity and the acceleration of the electron. These quantities are computed through the expectation values of their corresponding operators. In this master thesis the calculation of the operators and the implementation of the acceleration operator is only done in length gauge. In future work this will also be done in velocity gauge. The operator for the z-component of the N-electron position [17] is defined in Eq. (5), which can be expressed in spherical coordinates as

$$\hat{z} = \sum_{i=1}^{N} r_i \cos(\theta_i). \tag{8}$$

The z-component of the N-electron velocity operator is defined through using Ehrenfest theorem [15] as

$$\hat{v}_z = -i[\hat{z}, \hat{H}(t)] + \frac{\partial \hat{z}}{\partial t}, \tag{9}$$

where $\hat{H}$ is the time-dependent Hamiltonian expressed within length gauge. Since the position operator $\hat{z}$ is time independent, the velocity operator $\hat{v}_z$ becomes

$$\hat{v}_z = -\frac{i}{2}\sum_{i=1}^{N}[\hat{z}, \hat{p}_i^2]. \tag{10}$$

The derivation of the commutator is presented in Appendix A. The resultant expression is

$$\hat{v}_z = \sum_{i=1}^{N}\hat{p}_{z_i}, \tag{11}$$

which can be expressed in spherical coordinates as

$$\hat{v}_z = \sum_{i=1}^{N}\left(\cos\theta_i \frac{\partial}{\partial r_i} - \frac{\sin\theta_i}{r_i}\frac{\partial}{\partial \theta_i}\right). \tag{12}$$

Finally, the z-component of the N-electron acceleration operator is defined also through using Ehrenfest theorem as

$$\hat{a}_z = -i[\hat{v}_z, \hat{H}(t)] + \frac{\partial \hat{v}_z}{\partial t}, \tag{13}$$

which becomes

$$\hat{a}_z = iZ\sum_{i=1}^{N}\left[\hat{v}_z, \frac{1}{\vec{r}_i}\right] + iE(t)\sum_{i=1}^{N}[\hat{v}_z, z_i] - i\sum_{i>j}^{N}\left[\hat{v}_z, \frac{1}{|\vec{r}_i - \vec{r}_j|}\right]. \tag{14}$$

The derivation of the commutators is presented in Appendix A. The resultant expression is

$$\hat{a}_z = -Z\sum_{i=1}^{N}\frac{z_i}{r_i^3} - NE(t). \tag{15}$$

In spherical coordinates, the z-component of the N-electron acceleration is given by

$$\hat{a}_z = -Z\sum_{i=1}^{N}\frac{\cos(\theta_i)}{r_i^2} - NE(t). \tag{16}$$

The implementation of the operators given in Eqs. (8), (12) and (16) in the TDCIS methodology is described in Section 3.2.1 A.

2.1.3 Attosecond Transient Absorption

In the ATAS experiments the targeted quantity is the energy absorbed by the atom from the external field. This quantity is computed from the time-dependent operators described in the previous subsection. The derivation given here follows the work

presented in [7, 18]. Thus, the absorbed energy is calculated as the time integral of the energy change of the atom, it is given by

$$\Delta W = \int_{-\infty}^{\infty} dt \frac{d\Delta W}{dt} = \int_{-\infty}^{\infty} dt \frac{d}{dt} \langle \psi(t) | \hat{H}(t) | \psi(t) \rangle = \int_{-\infty}^{\infty} dt \langle \psi(t) | \frac{d\hat{V}(t)}{dt} | \psi(t) \rangle . \quad (17)$$

The instantaneous power absorbed by the atom, $\frac{d\Delta W}{dt}$, for the field interaction operators, presented in Eq. (4), is given by

$$\frac{d\Delta W}{dt} = \langle \psi(t) | \frac{d\hat{V}(t)}{dt} | \psi(t) \rangle = \begin{cases} z(t)\dot{E}(t); & \text{for LG,} \\ p_z(t)\dot{A}(t) + A(t)\dot{A}(t); & \text{for VG,} \end{cases} \quad (18)$$

where $z(t)$ and $p_z(t)$ are the expectation values of the operators $\hat{z}$ and $\hat{p}_z$ respectively.

In order to resolve the absorbed energy over frequency, the Fourier transform of the instantaneous power must be taken. The Fourier transform for a general function f is defined as

$$\begin{aligned} f(t) &= \frac{1}{\sqrt{2\pi}} \int \widetilde{f}(\omega) e^{-i\omega t} d\omega, \\ \widetilde{f}(\omega) &= \frac{1}{\sqrt{2\pi}} \int f(t) e^{i\omega t} d\omega. \end{aligned} \quad (19)$$

Thus, the Fourier transform of the instantaneous power in the length gauge (denoted by a (L) superscript) is given by

$$\begin{aligned} \Delta W^{(L)} &= \int z(t)\dot{E}(t) dt \\ &= \frac{1}{2\pi} \int \int \widetilde{z}(\omega) e^{-i\omega t} d\omega \int \widetilde{E}(\omega') \frac{d}{dt} e^{-i\omega' t} d\omega' dt \\ &= \frac{1}{2\pi} \int \int \widetilde{z}(\omega) \widetilde{E}(\omega') (-i\omega') \int e^{-i(\omega+\omega')t} dt d\omega d\omega' \\ &= -\frac{i}{2\pi} \int \int \omega' \widetilde{z}(\omega) \widetilde{E}(\omega') 2\pi\delta(\omega - (-\omega')) d\omega d\omega' \\ &= i \int \omega \widetilde{z}(\omega) \widetilde{E}(-\omega) d\omega \\ &= i \int \omega \widetilde{z}(\omega) \widetilde{E}^*(\omega) d\omega, \end{aligned} \quad (20)$$

where the relations $\int e^{i(k-k')x} dx = 2\pi\delta(k-k')$ and $f(t) \in \mathbb{R} \Rightarrow \widetilde{f}(\omega) = \widetilde{f}^*(-\omega)$ have been used. The latter relation can be used as the observables are real, time-dependent quantities. The integration over negative energies is removed as follows

$$\begin{aligned} \Delta W^{(L)} &= i \int_{-\infty}^{\infty} \omega \widetilde{z}(\omega) \widetilde{E}^*(\omega) d\omega \\ &= i \int_0^{\infty} \omega \widetilde{z}(\omega) \widetilde{E}^*(\omega) d\omega + i \int_{-\infty}^{0} \omega \widetilde{z}(\omega) \widetilde{E}^*(\omega) d\omega \\ &= i \int_0^{\infty} \omega \widetilde{z}(\omega) \widetilde{E}^*(\omega) d\omega - i \int_0^{\infty} \omega \widetilde{z}(-\omega) \widetilde{E}^*(-\omega) d\omega \\ &= -\int_0^{\infty} \omega 2 \frac{1}{2i} \left(\widetilde{z}(\omega) \widetilde{E}^*(\omega) - \widetilde{z}^*(\omega) \widetilde{E}(\omega) \right) d\omega \\ &= -2 \int_0^{\infty} \omega \, \mathrm{Im} \left\{ \widetilde{z}(\omega) \widetilde{E}^*(\omega) \right\} d\omega, \end{aligned} \quad (21)$$

where the expression has been simplified through using the relation $\mathrm{Im}\{f\} = \frac{f-f^*}{2i}$.

The description of the absorption in velocity gauge is reached by following the similar derivation steps, *see* [18]. The resultant expression is

$$\Delta W^{(V)} = -2\int_0^\infty \omega\,\mathrm{Im}\Big\{\widetilde{p}_z(\omega)\widetilde{A}^*(\omega) + \widetilde{A}(\omega)\widetilde{A}^*(\omega)\Big\}d\omega. \tag{22}$$

Since $A(\omega)A^*(\omega) = |A(\omega)|^2 \in \mathbb{R}$, the expression becomes

$$\Delta W^{(V)} = -2\int_0^\infty \omega\,\mathrm{Im}\Big\{\widetilde{p}_z(\omega)\widetilde{A}^*(\omega)\Big\}d\omega. \tag{23}$$

The frequency resolved energy in the two gauges is then

$$\frac{d\Delta W}{d\omega} = \begin{cases} -2\omega\,\mathrm{Im}\Big\{\widetilde{z}(\omega)\widetilde{E}^*(\omega)\Big\} & \text{for LG,} \\ -2\omega\,\mathrm{Im}\Big\{\widetilde{p}_z(\omega)\widetilde{A}^*(\omega)\Big\} & \text{for VG.} \end{cases} \tag{24}$$

2.1.4 Radiation

In the presence of an external field an atom will generate radiation due to the induced movement of the electron. The atomic response on the attosecond timescale, the timescale of electron motion, is of interest. On this timescale the movement of the nucleus is negligible due to its comparatively large mass. Therefore, only the movement of the electron will be considered. This section is based on the work presented in [19].

The radiation observed at a point $\vec{r}$, emitted by a moving point charge located at $\vec{r}_0$, is described by

$$\vec{E}_{rad}(\vec{r},t) = \frac{q\hat{n}\times[(c\hat{n}-\vec{v}(\tau))\times\vec{a}(\tau)]}{Rc^3(1-\beta_n)^3}, \tag{25}$$

where $\vec{R} = R\hat{n} = \vec{r} - \vec{r}_0(\tau)$ and $\beta_n = \dfrac{\vec{v}(\tau)\cdot\hat{n}}{c}$.

In the case of an initially stationary atom the equation is simplified since $\vec{v} = 0$. The assumption that the electron movement is directed only along the z-axis is used, yielding $\vec{a}(\tau) = a(\tau)\hat{e}_z$. As the radiation is emitted by the electron, $q = -1$. Expanding the triple cross product one arrives at

$$\vec{E}_{rad}(\vec{r},t) = \frac{-\hat{n}\times[\hat{n}\times\vec{a}(\tau)]}{c^2R} = \frac{\vec{a}(\tau) - \hat{n}[\vec{a}(\tau)\cdot\hat{n}]}{c^2R} = \frac{a(\tau)(\hat{e}_z - \hat{n}\cos\theta)}{c^2R}, \tag{26}$$

where θ is the angle between the two unit vectors $\hat{e}_z$ and $\hat{n}$. The radiation from a point charge accelerating in the z-direction is seen in Fig. 1, where both the magnitude and the polarisation direction of the radiation is shown. As seen, the polarisation direction is orthogonal to the propagation direction.

The energy radiated by a moving point charge can be calculated through the Poynting vector. In the following derivation the dependencies are removed for simplicity. The magnetic and electric radiation fields are related through $\vec{B}_{rad} = \frac{1}{c}\hat{n}\times\vec{E}_{rad}$. Thus,

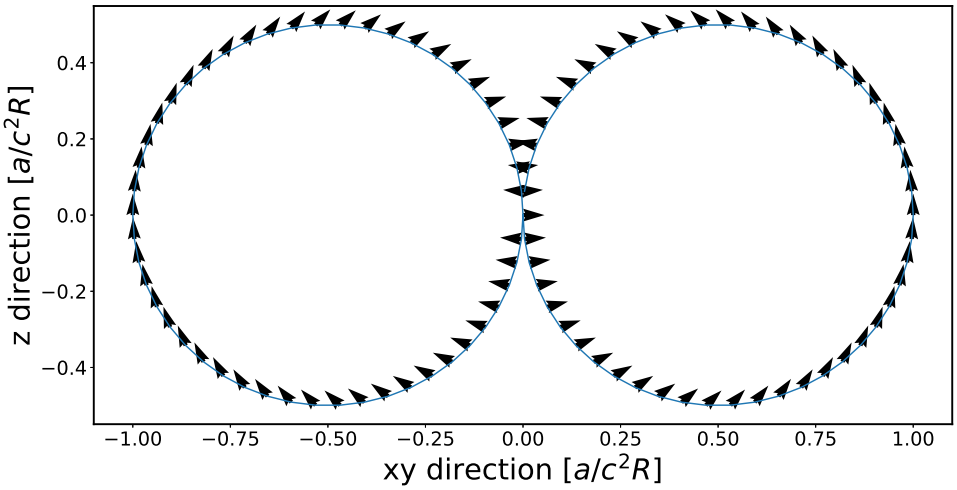

Figure 1: Radiation from an accelerating point charge. The magnitude in a direction is illustrated by the blue curve and the polarisation direction by the arrows

the Poynting vector becomes

$$\begin{aligned}
\vec{S} &= \frac{c^2 \vec{E}_{rad} \times \vec{B}_{rad}}{4\pi} \\
&= \frac{c}{4\pi} \vec{E}_{rad}^2 \hat{n} \\
&= \frac{c}{4\pi} \left(-\frac{\hat{n} \times [\hat{n} \times \vec{a}]}{c^2 R} \right)^2 \hat{n} \\
&= \frac{1}{4\pi c^3 R^2} (\hat{n} \times \sin(\theta) a \hat{m})^2 \hat{n} \\
&= \frac{\sin^2(\theta) a^2}{4\pi c^3 R^2} (\hat{n} \times \hat{m})^2 \hat{n} \\
&= \frac{\sin^2(\theta) a^2}{4\pi c^3 R^2} \hat{n},
\end{aligned} \tag{27}$$

where $|\vec{a}| = a$ and $\hat{m}$ is the unit vector which is normal to the plane containing $\hat{n}$ and $\vec{a}$. Thus, $\hat{m}$ and $\hat{n}$ are orthogonal, hence $(\hat{n} \times \hat{m})^2 = 1$.

The power per solid angle is given by

$$\frac{\partial P}{\partial \Omega} = R^2 \vec{S} \cdot \hat{n} = \frac{\sin^2(\theta) a^2}{4\pi c^3}, \tag{28}$$

while the total power radiated over all angles is

$$P = \frac{a^2}{4\pi c^3} \int_0^{\pi} \int_0^{2\pi} \sin^3(\theta) d\varphi d\theta = \frac{2a^2}{3c^3}. \tag{29}$$

Eq. (29) is the famous Larmor's formula, describing the power emitted by an accelerating point charge. Integration of Larmor's formula over time gives the total radiated energy W. Converting from time to frequency dependency as described in Eq. (20) one

arrives at

$$
\begin{aligned}
W &= \frac{2}{3c^3}\int a(t)^2 dt \\
&= \frac{2}{3c^3}\frac{1}{2\pi}\int\int \widetilde{a}(\omega)e^{-i\omega t}d\omega \int \widetilde{a}(\omega')e^{-i\omega' t}d\omega' dt \\
&= \frac{2}{3c^3}\frac{1}{2\pi}\int\int \widetilde{a}(\omega)\widetilde{a}(\omega')\int e^{-i(\omega+\omega')t}dt d\omega d\omega' \\
&= \frac{2}{3c^3}\int\int \widetilde{a}(\omega)\widetilde{a}(\omega')\delta(\omega-(-\omega'))d\omega d\omega' \\
&= \frac{2}{3c^3}\int_{-\infty}^{\infty} \widetilde{a}(\omega)\widetilde{a}(-\omega)d\omega \\
&= \frac{2}{3c^3}\left(\int_0^{\infty} \widetilde{a}(\omega)\widetilde{a}(-\omega)d\omega + \int_0^{\infty} \widetilde{a}(-\omega)\widetilde{a}(\omega)d\omega\right) \\
&= \frac{4}{3c^3}\int_0^{\infty} |\widetilde{a}(\omega)|^2 d\omega.
\end{aligned}
\tag{30}
$$

The frequency resolved energy emitted by a moving electron is

$$
\frac{\partial W}{\partial \omega} = \frac{4|\widetilde{a}(\omega)|^2}{3c^3}. \tag{31}
$$

Although this equation is calculated from the radiated field the expression is the same as for time-independent acceleration generating a classical field. Larmor's formula was first derived in the late 19th century and is entirely classical. It implies that all atoms are unstable as electrons should radiate energy as they accelerate around the nucleus. This was resolved with the discovery of quantum mechanics and Bohr's model of the atom. In Eq. (31) the connection to quantum mechanics is through the acceleration being the expectation value of the Hermitian operator given in Eq. (14). The TDSE, Eq. (1) used in our derivation, does not allow for spontaneous emission. Thus, the acceleration is non-zero only in the presence of an external field or when the atom is in a superposition with a dipole allowed transition i.e. where $|l - l'| = 1$ for the l quantum numbers of the two states.

2.2 Macroscopic Response

In this section, a macroscopic model based on interaction between single atoms is presented. The first step in the development of this model is the construction of a two-atom model, as seen in Section 2.2.1. This model couples two atoms either through dipole-dipole interaction or through the radiation fields generated by the atoms. The macroscopic many-atom model was constructed, as described in Section 2.2.2. In this model an external field is propagated through a one-dimensional sample. In the model the field interaction is described in the length gauge as the radiation field is calculated from the expectation value of the acceleration operator.

2.2.1 Two-Atom Model

The two-atom model describes the interaction between two atoms either through the dipole-dipole interaction or the interaction of the generated radiation fields. An approximation which is utilised is that the dipoles and any fields are directed along $\hat{\epsilon}_z$

and are orthogonal to the axis on which the atoms are placed $\hat{\epsilon}_x$. This geometry creates the largest coupling between atoms. Other geometries yield the same behaviour but on a longer time frame. For the radiation this can be seen in Eq. (26).

Using this model, one can simulate the interaction between an atom, which is initially in the ground state or a Rydberg state, with an atom in a superposition state. A superposition which has a dipole allowed transition will have non-zero expectation values for position, velocity and acceleration in the absence of an external field. As it is on these quantities that the interaction is dependent, this will induce interaction between the two atoms. As this model couples two atoms which are not in an external field, superpositions with dipole allowed transitions will be utilised to generate interaction between the atoms.

A Dipole-Dipole Interaction

The dipole-dipole interaction between two particles is

$$\hat{V}_{dip} = \frac{1}{R^3}(\hat{d}_1 \cdot \hat{d}_2 - 3(\hat{d}_1 \cdot \hat{n})(\hat{d}_2 \cdot \hat{n})), \tag{32}$$

where $\hat{d} = q\hat{\vec{r}}$ is the electric dipole moment operator, $\vec{R} = \vec{R_2} - \vec{R_1} = R\hat{n}$ is the distance between the two atoms positioned at $\vec{R_1}$ and $\vec{R_2}$ [20].

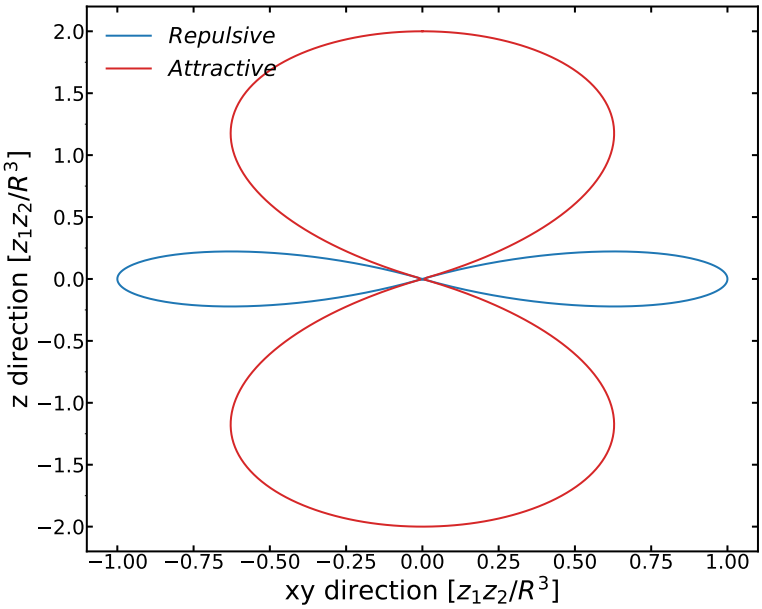

Figure 2: Dipole-dipole interaction from an atom with an electric dipole moment aligned along the z-direction.

The shape of the dipole-dipole interaction from an atom with a dipole aligned along the z-directions is illustrated in Fig. 2. The interaction is repulsive in the x-y plane and attractive above and below it. Placing the atoms on the x-axis creates the largest repulsive interaction between the atoms. Using this geometry, one arrives at the following simplified expression,

$$\hat{V}_{dip} = \frac{\hat{z}_1\hat{z}_2}{R^3}. \tag{33}$$

The dipole-dipole interaction couples two independent atoms with a dipole moment each. By using a mean field approach it can be approximated as a one body operator. The interaction is then calculated from a one-electron excitation in an atom, interacting with the dipole from the other atom. By using this approximation, the interaction for atom one can be written on the form

$$\hat{V}_{dip_1}(t) = \frac{z_2(\tau)}{R^3}\hat{z}, \tag{34}$$

where $z_2(\tau) = \langle \Psi_2(\tau)| \hat{z} |\Psi_2(\tau)\rangle$ is the expectation value of the electron position in atom two. It is dependent on the retarded time, $\tau = t - R/c$, to ensure that the interaction does not break causality by exceeding the speed of light.

The interaction operator in Eq. (1) will consist of two parts, the field interaction in length gauge, *see* Eq. (4), and the dipole-dipole interaction. The total interaction operator for atom one is thus

$$\hat{V}_1(t) = \hat{V}_{field}(t) + \hat{V}_{dip_1}(t) = E(t)\hat{z} + \frac{z_2(\tau)}{R^3}\hat{z} = \left(E(t) + \frac{z_2(\tau)}{R^3}\right)\hat{z}, \tag{35}$$

which is a real scalar multiplied with the position operator.

B Radiation Field Interaction

The radiation expression in Eq. (26) can be simplified using the established sample geometry. The radiation field emitted by atom two positioned at $\vec{r}_0(\tau) = R_2$ (note that the position is time-independent as the setup is stationary in this work) will be observed by atom one positioned at $\vec{r} = R_1$ as

$$\vec{E}_{rad} = \frac{a(\tau)\hat{\epsilon}_z}{c^2 R}. \tag{36}$$

The interaction for atom one can then be expressed in length gauge as

$$\hat{V}_{rad_1}(t) = \frac{a_2(\tau)}{c^2 R}\hat{z}, \tag{37}$$

where $a_2(\tau) = \langle \Psi_2(\tau)| \hat{a} |\Psi_2(\tau)\rangle$ is the expectation value of the electron acceleration in atom two at retarded time τ. The total interaction is thus

$$\hat{V}_1(t) = \hat{V}_{field}(t) + \hat{V}_{rad_1}(t) = \left(\vec{E}_{field}(t) + \vec{E}_{rad}(t)\right)\hat{z} = \left(E(t) + \frac{a_2(\tau)}{c^2 R}\right)\hat{z}, \tag{38}$$

which is the total electric field multiplied with the position operator.

Comparing the scaling of the dipole-dipole and acceleration induced radiation interaction one arrives at the expressions

$$\begin{aligned} \hat{V}_{rad} &\propto \frac{1}{c^2 R} \approx \frac{1}{10^4 R}, \\ \hat{V}_{dip} &\propto \frac{1}{R^3}, \end{aligned} \tag{39}$$

where the approximation that the expectation value of the position and acceleration is of the same order of magnitude has been made. Thus, the dipole-dipole interaction will dominate in the near field, whilst the radiation interaction will dominate in the far field.

2.2.2 Many-Atom One-Dimensional Model

The macroscopic many-atom sample is modelled as a cylinder divided up into slices (unit volumes) through which the external field can propagate as a plane wave. The atomic density is static, it follows a Gaussian distribution centred on the middle of the sample in order to mimic an electromagnetic pulse impinging on a gas jet. The single-atom response in a unit volume is multiplied by the population of the unit volume, calculated from the atomic density. The distance between unit volumes, and therefore also the length of the unit volumes, correspond to the distance the light travels in the chosen time step $\Delta L = c\Delta t$.

Pump-probe simulations are imitated by setting the atomic state of the unit volumes to an initially excited state. The same initial state is used in all unit volumes. This corresponds to a sample being excited by a pump pulse that follows the same trajectory as the propagating external field, which is the probe pulse. This is known as longitudinal pumping [10]. As the two pulses follow the same path the delay between them is the same for all unit volumes. Therefore, the states have developed the same amount when they interact with the external field.

A Field Propagation Through a Macroscopic Sample

A macroscopic model is developed through creating a one-dimensional like sample aligned along the x-axis separated into M_{max} unit volumes. Within the unit volume, the external field is diminished by the field generated by the macroscopic polarisation $\vec{P}$ in the unit volume. The local electric field [19] is described by

$$\vec{E}_{loc} = \vec{E} + \frac{\vec{P}}{3\epsilon_0}, \tag{40}$$

where $\vec{E}$ is the electric field which impinges on the unit volume. The polarisation is described by $\vec{P} = \rho\vec{d}$, where $\vec{d}$ is the electric dipole moment. The field induced by the polarisation accounts for the mean effects of dipole-dipole interaction. The field in unit volume M induced by the polarisation is thus

$$E_{in}(\tau) = \frac{-z_M(\tau)\rho_M}{3\epsilon_0}, \tag{41}$$

where ρ_M is the atomic density in unit volume M.

In addition to the induced field the unit volumes are coupled through the radiation fields created by the atoms. The radiation field in unit volume M is the sum of the radiated field from the previous unit volumes m. The fields emitted in the forward direction is emitted in phase. Radiation emitted in the backwards direction is neglected. The justification for this is that the fields cancel out as they are emitted out of phase, making it negligible compared to the radiation emitted in the forward direction. This can be seen in the results for the angular distribution of radiation in Fig. 24. Two models are presented for the propagation of the radiation field.

In the first model, the "atomic-line" model, all atoms are placed on a line as illustrated in Fig. 3. Each unit volume will then emit radiation in accordance with the single atom radiation profile shown in Fig. 1. The atomic-line model can be used to determine the radiation profile of the many atom sample.

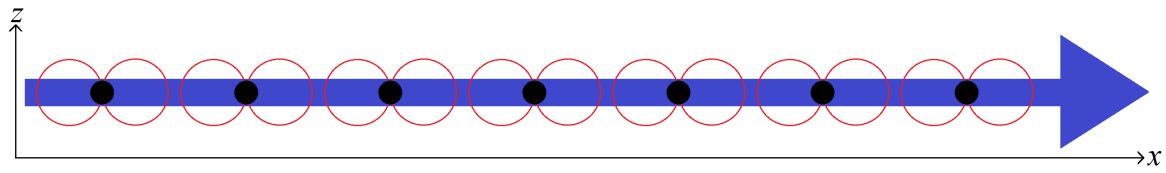

Figure 3: Illustration of the atomic-line model.

The radiation field observed by unit volume M is then described by

$$E^{line}_{rad_M}(\tau) = \sum_{m=1}^{M-1} E_{rad_m}(\tau) = \sum_{m=1}^{M-1} \frac{a_m(\tau)N_m}{c^2(M-m)\Delta L}, \tag{42}$$

where N_m is the population of unit volume m, calculated as the atomic density multiplied with the volume of the unit volume. The radiation produced in a unit volume is proportional to the inverse of the distance. In the model the distance between unit volumes M and m is $(M-m)\Delta L$.

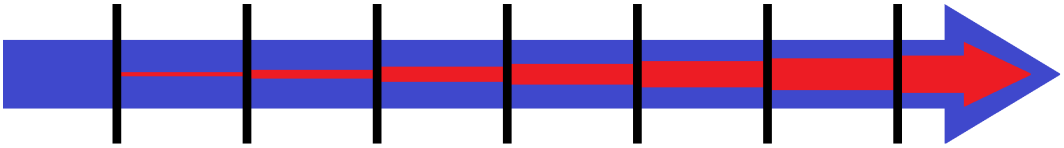

Figure 4: Illustration of the atomic-bulk model.

In the second model, the "atomic-bulk" model, one considers the atoms as being placed uniformly on parallel sheets, stretched orthogonally to the propagation direction. Each sheet corresponds to a unit volume. The sample is illustrated in Fig. 4. The atomic-bulk model can be used to determine the energy dissipated in the sample due to the propagation of the external field. The atoms on the sheet experience the same field, causing them to oscillate in phase. As in the case of the electric field from a uniformly charged plane, the generated radiation field is independent of distance. To mimic this one removes the R^{-1} scaling of the radiation field. The radiated field observed by unit volume M then becomes

$$E^{bulk}_{rad_M}(\tau) = \sum_{m=1}^{M-1} E_{rad_m}(\tau) = \sum_{m=1}^{M-1} \frac{a_m(\tau)N_m}{c^2}. \tag{43}$$

The total electric field in unit volume M then becomes

$$E_{tot_M}(\tau) = E_{ext}(\tau) + E_{in_M}(\tau) + E_{rad_M}(\tau), \tag{44}$$

where the radiation field can be modelled either through the atomic-line or the atomic-bulk model.

Retarded time is used to investigate the response of a unit volume in the time frame centred on that unit volume, defined as $\tau = t - \frac{x_M}{c}$, where x_M is the position of the unit volume of interest. Thus, a certain part of the external field will be observed by all unit volumes at the same retarded time. Radiation emitted by a unit volume at retarded time τ will be felt by the subsequent unit volumes at the same retarded time τ as the radiation will move along the exterior field. Note that the step size is the same in time and retarded time $\Delta t = \Delta\tau$. The electric fields and their respective retarded times are illustrated in the space-time diagram in Fig. 5.

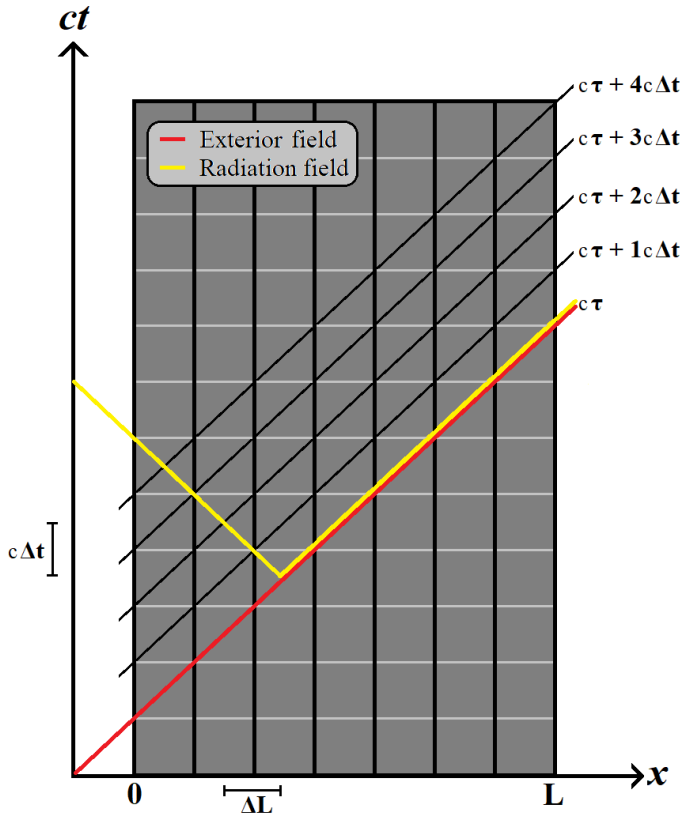

Figure 5: External and radiation fields and their dependence on space x, time t and retarded time τ. L is the sample size, ΔL is the spatial steps size and Δt is the step size in time. They are related through $\Delta L = c\Delta t$. Thus, it takes one unit of time for the pulse to move one unit of length, assuming the pulse travels with the speed of light in vacuum as the sample is diffuse.

B Radiation Emitted by Excited Macroscopic Sample

The radiation emitted by a macroscopic sample can be studied by the line model. From the acceleration expectation value in each unit volume the radiation in any direction can be calculated through Eq. (26). Due to the wave nature of the radiation field, the field from the different atoms can be added linearly. Thus, the electric field at a point $\vec{r}$ is given by

$$\vec{E}_{rad}(\vec{r},t) = \sum_{m=1}^{M_{max}} \vec{E}_{rad_m}(\vec{r},t) = \sum_{m=1}^{M_{max}} P(m) \frac{a\left(t - \frac{|\vec{r}-x_m\hat{\epsilon}_x|}{c}\right)\left(\hat{\epsilon}_z - \frac{(\vec{r}-x_m\hat{\epsilon}_x)}{|\vec{r}-x_m\hat{\epsilon}_x|}\cos\theta\right)}{c^2|\vec{r}-x_m\hat{\epsilon}_x|}. \tag{45}$$

The radiation generated by the macroscopic sample differs from the single-atom radiation. As the radiation is emitted by several oscillating atoms the total macroscopic radiation field will exhibit interference effects.

C Energy Dissipation of Field in a Macroscopic Sample

The total energy dissipated in the sample can be studied using the atomic-bulk model. It is the difference between the incoming and outgoing energy. This is described using the generated field, given by $\vec{E}_{gen} = \vec{E}_{in} - \vec{E}_{out}$, where $\vec{E}_{in}$ and $\vec{E}_{out}$ are the incoming and outgoing field respectively. The energy of the generated field is calculated from

the Poynting vector, which describes the directed energy per unit time and unit area. As the considered field is constant in the radial direction, since it is modelled as a plane wave, the power can be expressed through the Poynting vector as

$$P = \vec{S}\hat{n}_A A, \tag{46}$$

where A is an arbitrary area in the radial direction and $\hat{n}_A$ is the normal vector of the area, which points in the axial direction. Following the derivation presented in Section 2.1.4 the power becomes

$$P = \frac{cA}{4\pi}\vec{E}_{gen}(t)^2. \tag{47}$$

Converting from power to frequency resolved energy as described in Eqs. (30) and (31) one arrives at

$$\frac{\partial W}{\partial \omega} = \frac{cA}{2\pi}\left|\widetilde{E}_{gen}(\omega)\right|^2, \tag{48}$$

which is the total energy dissipated from the external field after propagation through the macroscopic sample. The results are normalised, removing the dependence on the area A.

3 Methodology

In this section the methodology for the calculation of the single and many-atom responses is presented. The atomic system is described physically through utilising the time-dependent configuration-interaction singles (TDCIS) method in Section 3.1. The Hartree-Fock method is described, the time-dependent wave functions are set up and the numerical methods used to propagate the wave functions are presented. The numerical methods used in the calculation of the observables and the simulation of the macroscopic response models described in the previous section are presented in Section 3.2.

3.1 Time-Dependent Configuration-Interaction Singles

In this section the methodology used in describing a single atom interacting with an external field is presented. The approach is based on the TDCIS method, which is built on the Hartree-Fock single-particle states (also called “spin orbitals”) [17]. By using the Hartree-Fock approximation one assumes that the atomic ground state can be described with a single Slater determinant. The electrons are affected by an average potential from the nucleus and other electrons. The Hartree-Fock equation is solved self-consistently to find the best single-particle states for describing the occupied spin orbitals in the ground state Slater determinant. In addition, unphysical unoccupied (also called ”virtual”) single-particle states are obtained through the Hartree-Fock method. The single-particle states determined by the Hartree-Fock calculation are then used to construct both the ground state Slater determinant and the singly excited Slater determinants, which together span the TDCIS wave function. This many-electron wave function can then be used to calculate the observables of the atom. The TDCIS wave functions are propagated through a second-order finite differencing scheme [14].

The TDCIS wave function is propagated by solving the TDSE for the N-electron wave function based on the Hartree-Fock ground and singly excited Slater determinants. In 3.1.1 the Hartree-Fock method is presented, in 3.1.2 the time-dependent Hamiltonian is utilised to construct the time-dependent wave function, in Section 3.1.3 the numerical scheme used to propagate the wave functions is presented and in Section 3.1.4 the limits of the TDCIS method is discussed. This section follows the book "Modern Quantum Chemistry" by A. Szabo and N. S. Ostlund [17] and the articles [14, 21].

3.1.1 Hartree-Fock Method

The Hartree-Fock method is a mean field method in which the N-electron problem is changed into N coupled one-electron problems. The wave function of an electron is given by the spin orbital $\chi(\vec{x})$, which depends on position and spin $\vec{x} = (\vec{r}, \sigma)$. If the electron-electron interaction is neglected, the N-electron Hamiltonian, $\hat{H}$, is the sum of N single-particle operators, h, where only the interaction with the nucleus and the electron kinetic energy is taken into account. Thus, the N-electron Hamiltonian is

$$\hat{H} = \sum_{i=1}^{N} \hat{h}(i), \tag{49}$$

where i is the electron index. In order to simplify the notation electron dependence of the operator will not be written out when it is acting on a state. The dependence of the operator will be the same as the dependence of the state on which it is operating. The spin orbital χ_k is calculated through solving the following eigenvalue problem,

$$\hat{h}\chi_k(\vec{x}_i) = \epsilon_k\chi_k(\vec{x}_i), \tag{50}$$

where ϵ_k is the spin orbital energy. As the N-electron Hamiltonian is the sum of the N $\hat{h}$ operators, the N-electron wave function can be expressed as the product of the spin orbitals. Since electrons are fermions, the antisymmetry principle has to be respected. Thus, the wave function must be antisymmetric with respect to the exchange of the coordinates of a pair of electrons, i.e.

$$\Psi(\vec{x}_1, \vec{x}_2 \cdots \vec{x}_m \cdots \vec{x}_n \cdots \vec{x}_N) = -\Psi(\vec{x}_1, \vec{x}_2 \cdots \vec{x}_n \cdots \vec{x}_m \cdots \vec{x}_N). \tag{51}$$

Therefore, one constructs Slater determinants as linear combinations of spin orbitals. Slater determinants are orthonormal and are given by

$$\Psi(\vec{x}_1, \vec{x}_2 \cdots \vec{x}_N) = (N!)^{-1/2} \begin{vmatrix} \chi_a(\vec{x}_1) & \chi_b(\vec{x}_1) & \cdots & \chi_k(\vec{x}_1) \\ \chi_a(\vec{x}_2) & \chi_b(\vec{x}_2) & \cdots & \chi_k(\vec{x}_2) \\ \vdots & \vdots & \ddots & \vdots \\ \chi_a(\vec{x}_N) & \chi_b(\vec{x}_N) & \cdots & \chi_k(\vec{x}_N) \end{vmatrix}. \tag{52}$$

In standard quantum chemistry textbooks, Slater determinants have the following shorthand notation,

$$|\Psi(\vec{x}_1, \vec{x}_2, \cdots, \vec{x}_N)\rangle = |\chi_a(\vec{x}_1)\chi_b(\vec{x}_2)\cdots\chi_k(\vec{x}_N)\rangle = |\chi_a\chi_b\cdots\chi_k\rangle\,, \tag{53}$$

see for example Ref. [17]. If two electrons exchange coordinates, the wave function, given by Eq. (52), changes sign. Also, if two electrons occupy the same spin orbital, two columns of the determinant are equal, making the wave function zero. This fact is in total accordance with Pauli exclusion principle which states that two fermions can not occupy the same state.

In the Hartree-Fock approximation, the Hartree-Fock spin orbitals $\{\phi_k\}$ are determined by solving the Hartree-Fock equation, which is given by

$$\hat{f}\phi_k(\vec{x}) = \epsilon_k\phi_k(\vec{x}), \tag{54}$$

where $\hat{f}$ is the Fock operator. This operator depends on the "mean field" potential generated by the other electrons. This approximation reduces the N-electron problem to N one-electron problems. The N lowest Hartree-Fock orbital energies, $\{\epsilon_k\}$ with $k \in \{a, b, c, \dots\}$ corresponds to the occupied orbitals. The rest corresponds to the unoccupied or virtual orbitals, for $k \in \{p, q, r, \dots\}$.

The Hartre-Fock ground state is thus given by the Slater determinant of the occupied orbitals,

$$|\phi_0\rangle = |\chi_1\chi_2\cdots\chi_a\chi_b\cdots\chi_N\rangle\,. \tag{55}$$

The energy of this state is $E_0 = \langle\phi_0|\,\hat{H}\,|\phi_0\rangle$. However, the exact ground state energy is $\mathscr{E}_0$. From the variational principle it is known that an approximate wave function always has a higher energy than the exact wave function. The electron correlation energy is defined as $E_{corr} = \mathscr{E}_0 - E_0$. This energy can therefore be seen as a measure of the quality of the Hartree-Fock method [17].

3.1.2 Time-Dependent Hamiltonian and Wave Functions

Excited states are described through exchanging an occupied spin orbital in the Slater determinant with a virtual one. A Slater determinant containing one virtual spin orbital is singly excited, if it contains two virtual spin orbitals it is doubly excited and so on. The notation used for a singly excited Slater determinant is,

$$\left|\phi_a^p\right\rangle = \left|\chi_1\chi_2\cdots\chi_p\chi_b\cdots\chi_N\right\rangle, \tag{56}$$

where the occupied spin orbital a has been exchanged with the virtual spin orbital p. The excited Slater determinants does not correspond to the excited states. However, they build up the basis function for a N-electron system.

The exact wave function $|\Phi\rangle$ can be calculated by summing over all Slater determinants i.e. the ground state, all permutations of the singly excited state, all permutations of the doubly excited state and so on up to the N times excited state. In order to limit the number of states treated the configuration interaction singles (CIS) approach is utilised. In this approach one approximates the exact wave function by the CIS states, constructed as linear combinations of the ground and all singly excited Slater determinants. The time-dependent wave function, $|\Psi(t)\rangle$, is obtained by solving the TDSE Eq. (1), it can be represented on the space of the CIS states as

$$|\Psi(t)\rangle = c_0(t)\,|\phi_0\rangle + \sum_{ap} c_a^p(t)\,\left|\phi_a^p\right\rangle, \tag{57}$$

where the expansion coefficients $c_0(t)$ and $c_a^p(t)$ are the time-dependent state amplitudes and $|\phi_0\rangle$ and $\left|\phi_a^p\right\rangle$ are the Hartree-Fock ground state and the singly excited state defined in Eq. (55) and Eq. (56), respectively.

The use of Eq. (57) to solve the TDSE is TDCIS method. Through inserting Eq. (57) into Eq. (1), the equations of motions for the time-dependent expansion coefficients can be written as

$$\begin{aligned} i\dot{c}_0(t) &= c_0(t)\,\langle\phi_0|\,\hat{H}(t)\,|\phi_0\rangle + \sum_{ap} c_a^p(t)\,\langle\phi_0|\,\hat{H}(t)\,\left|\phi_a^p\right\rangle, \\ i\dot{c}_a^p(t) &= c_0(t)\,\left\langle\phi_a^p\right|\,\hat{H}(t)\,|\phi_0\rangle + \sum_{bq} c_b^q(t)\,\left\langle\phi_a^p\right|\,\hat{H}(t)\,\left|\phi_b^q\right\rangle. \end{aligned} \tag{58}$$

The required matrix elements in Eq. (58) can be calculated using the Slater-Condon rules [17]. A summary of the Slater-Condon rules and the derivation of said matrix element is given in Appendix B. Finally, through using the selection rules of the interaction operator, the time-dependent expansion coefficients are written in terms of the spin orbitals as follows:

$$\begin{aligned} i\dot{c}_0(t) &= \sum_{ap} c_a^p(t)\,\langle\chi_a|\,\hat{v}(t)\,|\chi_p\rangle, \\ i\dot{c}_a^p(t) &= c_0(t)\,\langle\chi_p|\,\hat{v}(t)\,|\chi_a\rangle + c_a^p(t)(\epsilon_p-\epsilon_a) + \sum_q c_a^q(t)\,\langle\chi_p|\,\hat{v}(t)\,|\chi_q\rangle \\ &\quad - \sum_b c_b^p(t)\,\langle\chi_b|\,\hat{v}(t)\,|\chi_a\rangle + \sum_{bq} c_b^q(t)[2\,\langle\chi_p\chi_a|\chi_b\chi_q\rangle - \langle\chi_p\chi_q|\chi_b\chi_a\rangle], \end{aligned} \tag{59}$$

where the two-electron integrals are given by

$$\langle\chi_i\chi_j|\chi_k\chi_l\rangle = \int d\vec{x}_1 d\vec{x}_2 \chi_i^*(\vec{x}_1)\chi_j^*(\vec{x}_2)\frac{1}{|\vec{r}_1-\vec{r}_2|}\chi_k(\vec{x}_1)\chi_l(\vec{x}_2). \tag{60}$$

3.1.3 Numerical Resolution of the Equations of Motion

In order to solve Eq. (59) at each time step, the second-order finite differencing scheme (SOD) was used [21]. The SOD was defined as

$$\Psi(t+\Delta t) = \Psi(t-\Delta t) - 2i\Delta t\hat{H}(t)\Psi(t). \tag{61}$$

IF the hamiltonian is hermitian this propagation preserves the norm of the wave function.However, in the present work an exterior complex scaling (ECS) potential has been implemented in order to avoid reflections during time propagation [22]. As a consequence, the Hamiltonian becomes non-hermitian and the norm of the wave function will be decreased, absorbed at the end of the simulation box. This aims to reproduce the possible ionisation of the system. The propagation will be stable if the following criterion for the time step is fulfilled

$$\Delta t < \frac{2\pi}{\epsilon_{max}}, \tag{62}$$

where ϵ_{max} is the largest absolute eigenvalue of the Hamiltonian. In order to make sure that the criterion is fullfilled the maximum energy is selected to be more than twice the central frequency of the external field. The error per time step is proportional to Δt^3 [21]. Following the work presented in references [14, 23], Eq. (59) is rewritten as

$$\begin{aligned} c_0(t+\Delta t) &= c_0(t-\Delta t) - 2i\Delta t \sum_{ap} c_a^p(t) \left\langle \chi_a \right| \hat{v}(t) \left| \chi_p \right\rangle, \\ c_a^p(t+\Delta t) &= e^{-2i(\epsilon_p-\epsilon_a)\Delta t} c_a^p(t-\Delta t) - 2i\Delta t e^{-i(\epsilon_p-\epsilon_a)\Delta t} f_a^p(t), \end{aligned} \tag{63}$$

where

$$\begin{aligned} f_a^p(t) = c_0(t) \left\langle \chi_p \right| \hat{v}(t) \left| \chi_a \right\rangle + \sum_{bq} c_b^q(t) [2 \left\langle \chi_p \chi_a \right| \chi_b \chi_q \rangle - \left\langle \chi_p \chi_q \right| \chi_b \chi_a \rangle] \\ + \sum_q c_a^q(t) \left\langle \chi_p \right| \hat{v}(t) \left| \chi_q \right\rangle - \sum_b c_b^p(t) \left\langle \chi_b \right| \hat{v}(t) \left| \chi_a \right\rangle. \end{aligned}$$

The transition matrix elements are solved as described in Appendix C.

3.1.4 Gauge Dependence of the TDCIS Method

The TDCIS method has limits stemming from the fact that the time-dependent wave function is expanded in a truncated Hilbert space, i.e. the space of single excitations (the CIS basis). As illustrated in Fig. 6, the consequences of this approximation can be seen in the instantaneous electron population of the ground state of helium. The electron population is computed in length gauge and velocity gauge in hydrogen (a) and helium (b). As seen, the final population in hydrogen agrees between the different gauges, hence, the result is gauge invariant. In helium however, the final population is not gauge invariant. This is true not only for the population, but for all observables. This is because the CIS basis is not exact for many-electron atoms. In order to reproduce correct observables in many-electron systems, electron correlation must be included.

In addition, note that observables are not gauge invariant during the interaction with the electric field in both hydrogen and helium. This is a well known issue explained in different textbooks on quantum mechanical, *see* for example [15]. one has

to be careful with what conclusions are drawn from the instantaneous time-dependent expectation values. After the interaction with the electric field, the properties will be gauge invariant. For example, the instantaneous power transfer to the hydrogen atom is gauge variant, whilst the total energy gain of the atom, is gauge invariant. This is discussed further in [24].

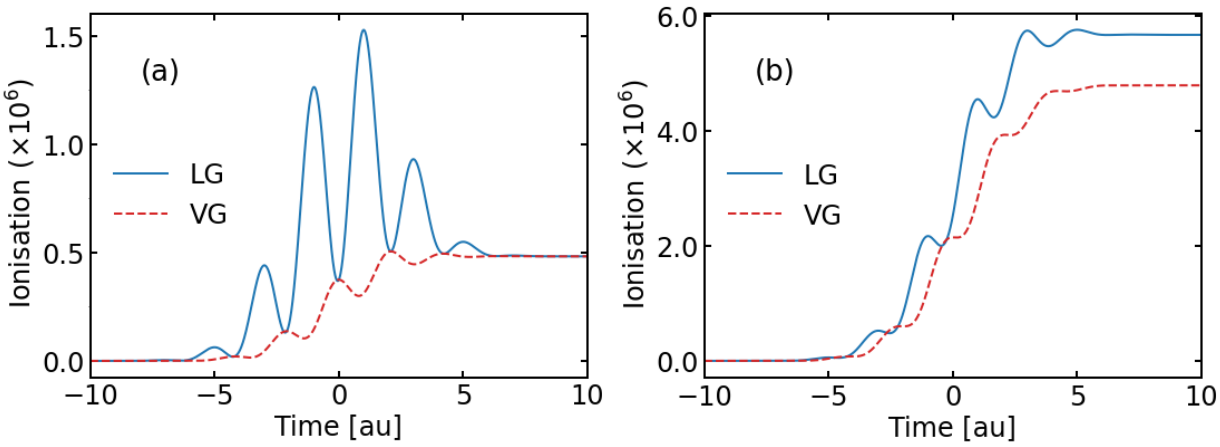

Figure 6: A comparison of the ionisation of an atom in the ground state interacting with an attosecond pulse, calculated in length gauge and velocity gauge in hydrogen (a) and helium (b).

3.2 Numerical Methods and Computational Details

In this section the numerical methods used to implement the various models are presented. In Section 3.2.1 computational details of the single-atom model are presented, showing the computation of the operators as well as the state population for the beyond hydrogen case. In Sections 3.2.2 and 3.2.3 the numerical methods used to implement the two-atom model and the many-atom model are presented respectively.

The simulation of the single-atom response, the two-atom model and the many-atom model were conducted in Fortran. All the simulated data was analysed using Python.

3.2.1 Single-Atom Model

The subroutines for the single-atom model were in place previously to this master thesis with the exception of the implementation of the computation of the expectation value of the acceleration, described in A and the computation of the state population in the beyond hydrogen case described in B.

I implemented the computation of the acceleration expectation value into the existing subroutine which calculates the position and velocity expectation values. It was implemented in a similar way to the position expectation value as they both have the same angular dependence, *see* Table 1.

The subroutines used to calculate the state population in the beyond hydrogen case were written but not implemented previously to this master thesis. Initially the state population was calculated for the relativistic case, I modified it to handle the non-relativistic case and implemented the subroutine into the code.

A Numerical Computations of the Operators

The operators of position, velocity and acceleration given by Eqs. (8), (12) and (16) respectively are one-body operators that can be generalised with the following one-body operator formula:

$$\hat{\mathcal{O}} = \sum_{i=1}^{N} \hat{o}(i) = \sum_{i=1}^{N} f_i(r) g_i(\theta, \varphi), \tag{64}$$

where $f_i(r)$ and $g_i(\theta, \varphi)$ are general functions depending on the radial and angular coordinates of electron i respectively. The radial and angular parts of the operators are presented in Table 1.

Table 1: Radial and angular parts of the position, velocity and acceleration operators. The second term in the acceleration operator Eq. (16) has neither radial nor angular dependencies and can therefore simply be added to the expectation value.

Operator term	Radial part $f(r)$	Angular part $g(\theta, \varphi)$
$\hat{z}$	r	$\cos\theta$
$\hat{v}_z$ term 1	$\frac{\partial}{\partial r}$	$\cos\theta$
$\hat{v}_z$ term 2	$\frac{1}{r}$	$\sin\theta \frac{\partial}{\partial\theta}$
$\hat{a}_z$	$-\frac{Z}{r^2}$	$\cos\theta$

The time-dependent expectation value of Eq. (64) for the wave function in Eq. (57) is given by

$$\begin{aligned}\langle\Psi(t)|\,\hat{\mathcal{O}}\,|\Psi(t)\rangle = c_0^*(t)c_0(t)\,\langle\phi_0|\,\hat{\mathcal{O}}\,|\phi_0\rangle + \sum_{bq} c_0^*(t)c_b^q(t)\,\langle\phi_0|\,\hat{\mathcal{O}}\,|\phi_b^q\rangle \\ + \sum_{ap} c_a^{p*}(t)c_0(t)\,\langle\phi_a^p|\,\hat{\mathcal{O}}\,|\phi_0\rangle + \sum_{abpq} c_a^{p*}(t)c_b^q(t)\,\langle\phi_a^p|\,\hat{\mathcal{O}}\,|\phi_b^q\rangle\,,\end{aligned} \tag{65}$$

where the first term is zero due to the selection rules. The other terms are expanded using the Slater-Condon rules and relations presented in Appendix B except for the second term in the acceleration operator as it is a scalar. The resulting transition matrix elements are identical to Eq. (97) in Appendix C and the radial transition matrix elements are computed using the B-spline as described in that appendix. The angular transition matrix elements are calculated using the Wigner-Eckart theorem [25] as follows:

$$\begin{aligned}&\langle lm|\cos\theta\,|l'm'\rangle = (-1)^m\sqrt{(2l+1)(2l'+1)}\begin{pmatrix} l & 1 & l' \\ -m & 0 & m'\end{pmatrix}\begin{pmatrix} l & 1 & l' \\ 0 & 0 & 0\end{pmatrix}, \\ &\langle lm|\sin\theta\frac{\partial}{\partial\theta}\,|l'm'\rangle = \\ &= \sqrt{(2l+1)(2l'+1)}\Bigg[(-1)^m m\begin{pmatrix} l & 1 & l' \\ -m & 0 & m'\end{pmatrix}\begin{pmatrix} l & 1 & l' \\ 0 & 0 & 0\end{pmatrix} \\ &+ (-1)^{m'+1}\sqrt{(l'-m')(l'+m'+1)}\begin{pmatrix} l & 1 & l' \\ -m & -1 & m'+1\end{pmatrix}\begin{pmatrix} l & 1 & l' \\ 0 & 0 & 0\end{pmatrix}\Bigg].\end{aligned} \tag{66}$$

where the (2×3) arrays are the Wigner 3-j symbols [25].

B State Populations in TDCIS

In the case of hydrogen, the one-electron problem with a Coulomb potential is diagonalized in order to obtain the actual states of the hydrogen atom. However, in the beyond-hydrogen case, the computed CIS states are approximate. In order to compute the actual state populations, one has to project the states on the eigenstates of the CIS Hamiltonian. Diagonalization of the CIS Hamiltonian yields the CIS energies ϵ_i and the CIS states

$$|\mathrm{CIS}_i\rangle = k_{i0}\,|\phi_0\rangle + \sum_{ap} k_{ia}^{p}\,|\phi_a^p\rangle\,, \tag{67}$$

as its eigenvalues and eigenvectors respectively. The population of the physical state (denoted by i) is given by the absolute square of the projection of the propagating wave function Eq. (57) on the eigenstates of the Hamiltonian

$$\begin{aligned}
|\beta_i(t)|^2 &= \langle \mathrm{CIS}_i|\Psi(t)\rangle \\
&= \left|\left(k_{i0}^{*}\,\langle\phi_0| + \sum_{ap} k_{ia}^{p*}\,\langle\phi_a^p|\right)\left(c_0(t)\,|\phi_0\rangle + \sum_{bq} c_b^q(t)\,|\phi_b^q\rangle\right)\right|^2 \\
&= \left|k_{i0}^{*}c_0(t)\,\langle\phi_0|\phi_0\rangle + \sum_{ap}\sum_{bq} k_{ia}^{p*}c_b^q(t)\,\langle\phi_a^p|\phi_b^q\rangle\right|^2 \\
&= \left|k_{i0}^{*}c_0(t) + \sum_{ap} k_{ia}^{p*}c_a^p(t)\right|^2,
\end{aligned} \tag{68}$$

where the fact that the Hartree-Fock orbitals are orthonormal have been utilised.

3.2.2 Two-Atom Model

This model is used to investigate the interaction of two atoms. In this master thesis, the model is used to couple one atom in a single state to an atom in a superposition state with a dipole allowed transition, this is illustrated in Fig. 7(a). The structure of the code used to implement the two atom model is presented in Fig. 7(b). I implemented the two-atom model by writing a Linux shell script that initiates two Python codes. The python codes define the simulation parameters of the two atom separately. Each Python program initialises a Fortran simulation which simulate a single-atom. The Fortran scripts run in parallel. They are based on the previously existing single-atom code, which propagates the atomic state based on the interaction with an external field and computes the expectation value of the observables which depend on the atomic state.

I used the single-atom code as a starting point and developed the two-atom model code from it. In the two-atom model code, the observables are used to calculate the interaction with the other atom. The interaction calculated from atom one's observables is then used as the external field used to propagate the state of atom two and vice versa. Each simulation is connected to two files, atom one writes its outgoing field into the file which atom two reads its incoming field from. Atom two writes its output into the second file and atom one reads that file as its input. Care is taken to make sure that interaction is read in the correct time step, dependent on the distance between the atoms through the retarded time. The simulation is set up so that the dipole of the atom in a superposition state is zero at $t = 0$.

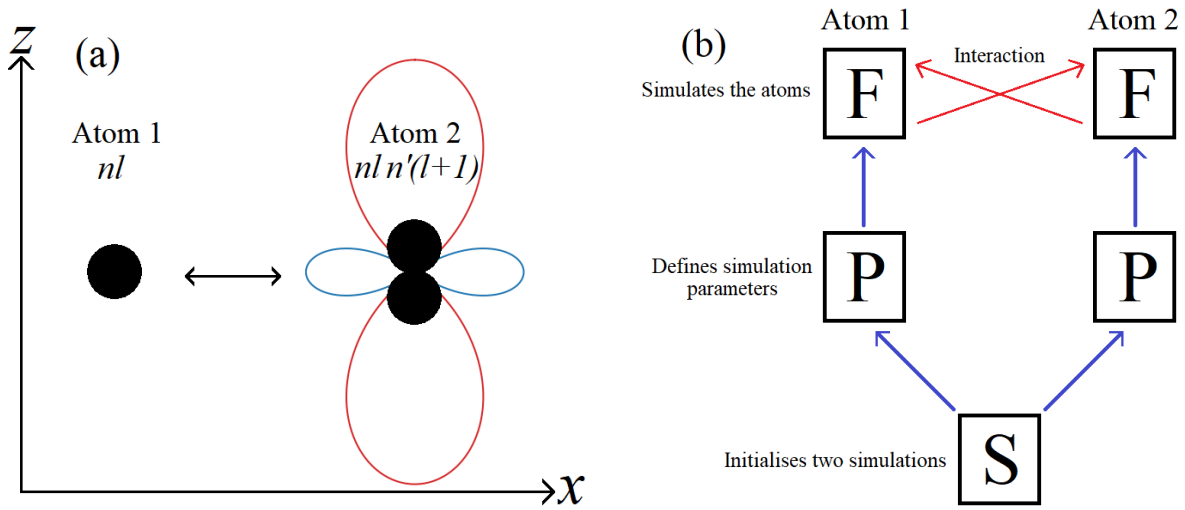

Figure 7: (a) Illustration of the two atom model showing Atom 1 in a single state $(n\ell)$ interacting with Atom 2 which is prepared in a state superposition $(n\ell;n'[\ell+1])$. The total dipole allowed transition in Atom 2 induces the interaction between the two atoms. (b) Schematic representation of the two-atom model code implemented in this work. The capital letters S, P and F denote different subroutines written in bash-shell, python and Fortran 90 languages, respectively. The blue arrows show the initialisation of programs and the red arrows represent the interaction between the two single-atom simulations.

One can define the distance between the atoms. The interaction type can be set to either dipole-dipole interaction or radiation interaction. The atomic type and initial state of the two atoms is defined separately. The two atoms can be simulated with or without an external field, defined separately for the two atoms.

3.2.3 Many-Atom Model

The many-atom model code I have written is based on the previously existing single-atom code. The sample is illustrated in Fig. 8. It is set up as a sequence of unit volumes, each with a population calculated from the defined Gaussian atomic density. The unit volumes are simulated as a single atom, with the response scaled by the unit volume population. The unit volumes are simulated in in the order in which they interact with the external field. As only radiation emitted in the forward direction is used in the propagation, for simplicity the entire time range of a unit volume is simulated before moving to the next unit volume, where the radiation from the previous unit volume is used as input. In each time step, the acceleration expectation values are saved to a matrix, ordered as unit volume against time.

The many-atom fields are calculated as follows. The induced field is calculated from the position expectation value dependent on the atomic state in the current unit volume in each time step. This is an approximation as the polarisation should be an instantaneous effect of the external field, rather it is computed from the position expectation value which is dependent on the electric field in the previous time step. For small time steps, such as those used in this work, the discrepancy should be negligible as the difference in position expectation value is small between times steps. The radiation field is calculated as the sum of the incoming radiation fields, calculated from the

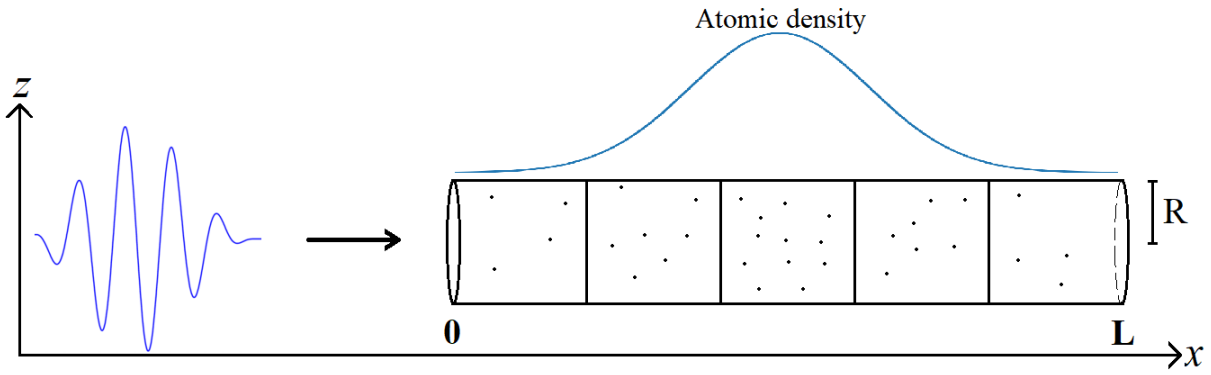

Figure 8: Schematic representation of the many-atom model showing the cylindrical sample of length L and radius R. The sample is divided up into a number of unit volumes and the atomic density in the sample follows a normal distribution. The black arrow indicates the propagation direction of the external electric field.

acceleration expectation values in the previous unit volumes, emitted at the current interaction time. This is the case as the distance between the unit volumes is $\Delta L = c\Delta t$ where Δt is the length of the time step. The total field, which is the sum of the external, induced and radiation fields, is used to propagate the atomic state.

As the time steps used are small, the unit volume lengths will be small as well. Thus, many unit volumes will have to be handled in order to simulate a macroscopic sample. In order to reduce the computational time one can separate the sample into a number of segments. For each of the segments only one of the unit volumes is populated by the sum of the population in the segment. The unit volume which is populated is defined as the position of average population in the segment, calculated by

$$M_{mean} = \frac{\sum_{m=M_l}^{M_h} N_m m}{\sum_{m=M_l}^{M_h} N_m}, \tag{69}$$

where the segment has the lower and higher bound M_l and M_h respectively, N_m is the population of unit volume m. The result is rounded to the nearest integer. All other unit volume are empty and not solved for. Thus, the number of simulations is reduced from the number of unit volumes to the number of segments. The validity of this approximation can be investigated by checking the convergence of the results with respect to the number of segments.

Finally,hpresent e acceleration in each unit volume can be used to calculate the macroscopic radiation at any point $\vec{r}_{det}$ through Eq. (45). The detection time of the radiation emitted from unit volume M at retarded time τ_e is calculated as

$$T(\vec{r}; M, \tau_e) = \tau_e + \frac{x_M - x_0 + |\vec{r}_{det} - x_M \hat{\epsilon}_x|}{c}. \tag{70}$$

The detection time is the sum of the time for the external field to reach unit volume M, the retarded emission time and the time for the radiation field to reach the detection point.

4 Results and Discussion

In this section the results are presented along with discussion. In Section 4.1 the single-atom response results are presented. These results are simulated for a single atom interacting with an attosecond pulse. The investigated properties are the observables of the atom, computed from the atomic state. From the observables one calculates the absorption and radiation. In Section 4.2 the two-atom model results are presented. In these results two atoms are coupled; atom one, initially in the ground state or a Rydberg state, is coupled to atom two, in a superposition of Rydberg states. The superposition has a dipole allowed transition, which is resonant to a transition in atom one. The coupling is modelled either as dipole-dipole interaction, *see* Section 2.2.1A, or radiation interaction, *see* Section 2.2.1B. The investigated aspects are the population and the observables of the atoms. From this the effect of the two interactions is investigated. For the simulation setup described, it is the Förster resonance energy transfer which is observed for the dipole-dipole interaction and excitation with a resonant field in the case of the radiation interaction. In Section 4.3 the many-atom model results are presented. These simulations model an attosecond pulse propagating through a macroscopic sample. The fields, both induced and radiation, are the properties of interest and are used to investigate the propagation and the emitted radiation field as well as the dissipated energy.

Throughout most of the present results, except where it is noted, hydrogen atoms are investigated. Because of this, the approximations made by the TDCIS method will not affect the results.

4.1 Single-Atom Response

Here the results of the single-atom response to a perturbation generated by an attosecond pulse is presented. In Section 4.1.1 the expectation values of the observables induced by the external field are presented and compared to the corresponding derivatives. In Sections 4.1.2 and 4.1.3 the attosecond transient absorption spectra and radiated energy spectra are presented respectively. These are simulated for a single atom in a superposition of states interacting with an attosecond pulse, the results are resolved over the relative wave-packet phase of the superposition.

These are the parameters used for all single-atom response simulations except where noted. An attosecond pulse, described by Eq. (7) modelled with $A_0 = 10^{-3}$ au, $\omega_0 = 1.5$ au ≈ 40.8 eV and $\tau_e = 5$ au ≈ 121 as, interacts with a hydrogen atom in the ground state. The interaction was modelled in length gauge in order to investigate the expectation value of the acceleration operator. The B-spline basis, described in Appendix 3.1.3, was defined with the following number of knot points in each region: $n_{inner} = 2$, $n_{linear} = 200$ and $n_{ECS} = 20$, the linear spacing $dR_{linear} = 0.5$ au, the complex scaling angle $\theta_{ECS} = 15^\circ$ and the polynomial order $k_s = 8$. The maximum l quantum number for the excited electrons was $l_{max} = 8$ and the maximum energy of the CIS states was $\epsilon_{max} = 16$ au. Time was discretized in the interval -20 au to 20 au with a step size of 0.01 au ≈ 0.241 as.

4.1.1 Observables of Atom Interacting with Attosecond Pulse

In this section, the simulated reaction is H + $\gamma \rightarrow$ H*. The simulation is conducted in order to investigate the observables of the excited atom. In Fig. 9 the expectation

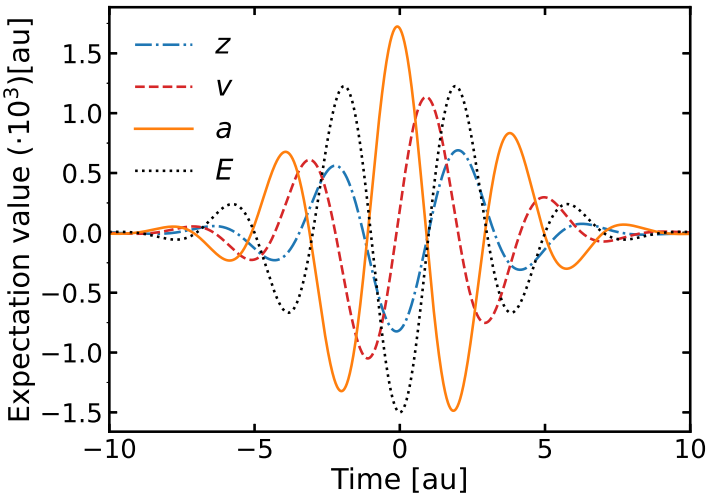

Figure 9: Expectation values of position, velocity and acceleration as well as the electric field. The results were simulated for a hydrogen atom in the ground state interacting with an attosecond pulse. The observables were computed as the expectation value of the corresponding operators.

values of the dipole position, velocity and acceleration as well as the electric field are presented. The acceleration has a similar shape to what is expected in classical physics, since classically acceleration is proportional to the force. The force in turn is proportional to the negative electric field for a negatively charged particle, such as an electron. There is the typical $\pi/2$ shift between the position and velocity as well as the velocity and the acceleration.

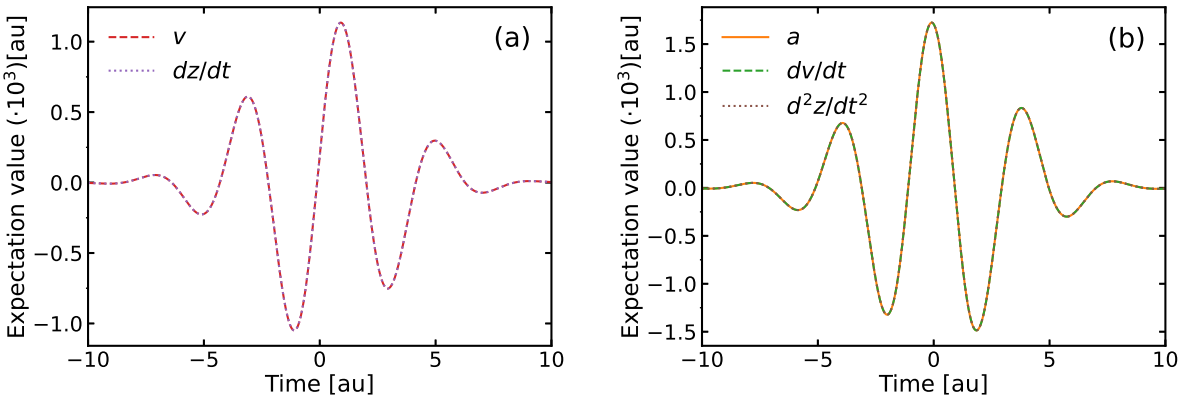

Figure 10: Velocity (a) and acceleration (b) compared to their corresponding derivatives. The results were simulated for a hydrogen atom in the ground state interacting with an attosecond pulse. The observables were computed as the expectation value of the operators and the time derivatives computed as the numerical derivatives of the observables.

In Fig. 10 the observables are compared to the corresponding derivatives. In (a) the

expectation value of the velocity is compared with the numerically computed derivative of the position. The two curves overlap as expected. In (b) the expectation value of the acceleration is compared with the derivative of the velocity and the second derivative of the position. Also, here the curves overlap as expected. From these results it is clear that the position, velocity and the acceleration are consistent with each other and suggest that the implementation of the computation of the acceleration expectation value is correct.

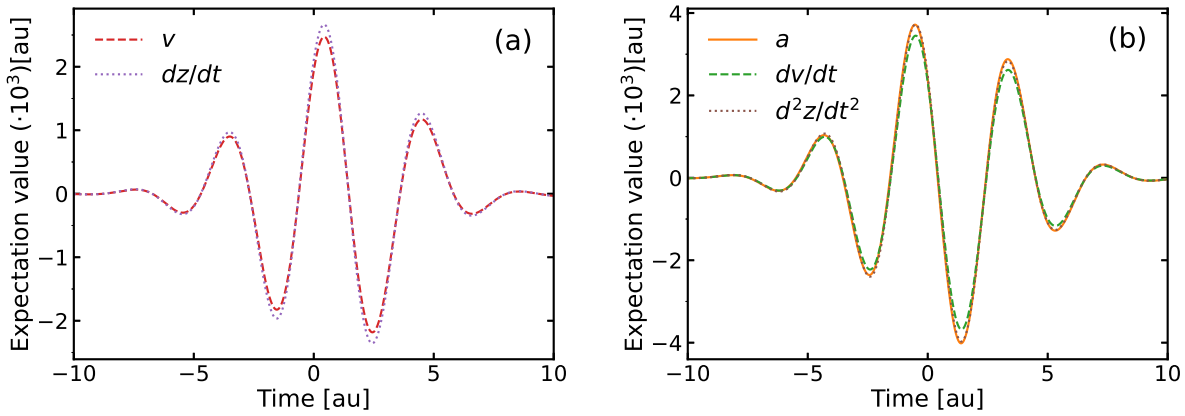

Figure 11: Velocity (a) and acceleration (b) compared to their corresponding derivatives. The results were simulated for a helium atom in the ground state interacting with an attosecond pulse. The observables were computed as the expectation value of the operators and the time derivatives were computed as the numerical derivatives of the observables.

In Fig. 11 the attosecond pulse is interacting with a helium atom in the ground state. In order to better describe the helium atom the number of knot points in the inner region was changed to $n_{inner} = 20$. In (a) the expectation value of the velocity is compared with the numerically computed derivative of the position and in (b) the acceleration is compared to the first derivative of the velocity and the second derivative of the position expectation values. The figure shows that there is a discrepancy between the curves in both cases. This is not a physical effect but rather a consequence of the CIS basis being an approximation of the real wave function, which is discussed in Section 3.1.4.

4.1.2 ATAS of Hydrogen Atom in a Superposition State

In this section the reaction H* + $\gamma \rightarrow$ H*′ was simulated in order to investigate the energy absorption of an atom from an electric field. Rather than defining several pulses to interact with the atom, pump-probe simulations were conducted through defining an initial superposition state of the atom interacting with an external field. As this renders the delay time superfluous, it is set to $t_0 = 0$. This is an idealized way of doing pump-probe simulations, as one assumes that one can use the pump pulse to excite to exactly the state which one wants to investigate. The influence of the relative wavepacket phase of the superposition is investigated by scanning over the phase. This is done through varying the state amplitudes of a superposition state. For an equally populated superposition of two states, with amplitudes complex amplitudes c_1 and

c_2, one has the relation

$$\begin{aligned} c_1 &= 2^{-\frac{1}{2}}, \\ c_2 &= 2^{-\frac{1}{2}}\, e^{i\varphi} e^{i(\omega_1-\omega_2)t}, \end{aligned} \tag{71}$$

where φ is the relative phase, ω_1 and ω_2 are the energies of the two states and t is time. Thus, one can resolve the response of an atom with regards to the relative phase through varying the state amplitudes. In the more fundamental, non-ideal approach, where one instead defines two pulses, to pump and probe the atom, the phase of the interaction would then be controlled through the delay between the two pulses as $\varphi = (\omega_1 - \omega_2)\Delta t_0$, where Δt_0 is the delay time between the pulses. The relative wave-packet phase between the states was scanned over the entire range of values, from π to $-\pi$, in 121 steps.

The simulations were conducted in velocity gauge, in order to more easily compare with the previeous investigations in [18] which were conducted in velocity gauge. Three different central frequencies where used $\omega_0 = \{1.5, 4.5, 15\}$ au. The parameters were changed to allow for the higher excitation energies. The maximum energy for the CIS states was changed to $\epsilon_{max} = 30$ au, the maximum l number of the excited electrons was reduced to $l_{max} = 6$ in order to limit the computational time. The number of knot points in the linear region was changed to $n_{linear} = 400$.

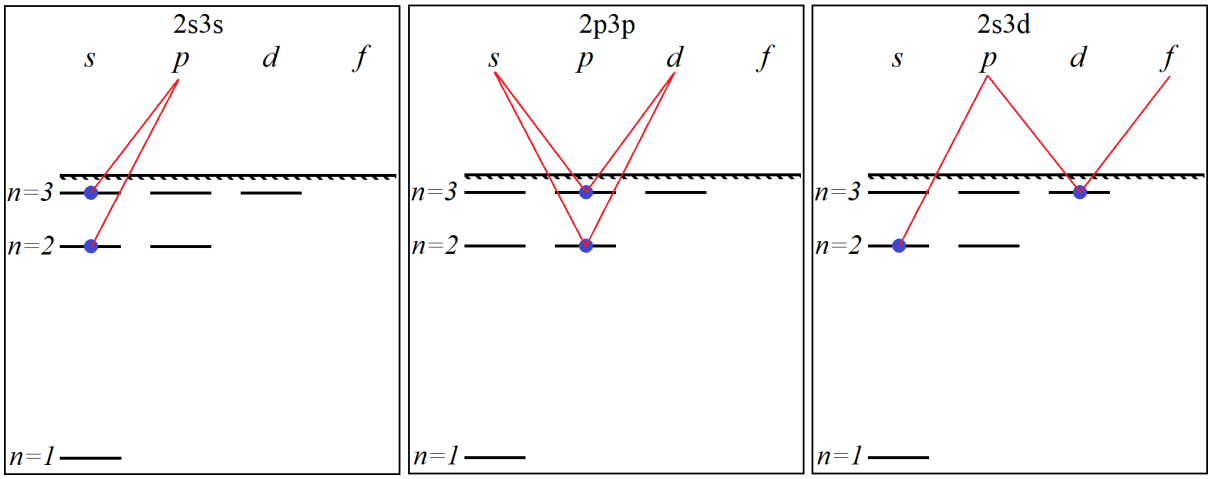

Figure 12: Level schemes of the possible transitions for the superpositions 2s3s, 2p3p and 2s3d in the left, middle and right panels respectively. The occupied states are represented by blue dots and the possible transitions are represented by red lines.

ATAS maps for three different superopositions are presented 2s3s, 2p3p and 2s3d, the level schemes and possible transitions of these superpositions are illustrated in Fig. 12. In Fig. 13 nine ATAS maps are shown. The superposition states 2s3s, 2p3p and 2s3d are presented in the top, middle and bottom row respectively. Three central frequencies of the external field were simulated 1.5 au, 4.5 au and 15 au, these are presented in the left, middle and right column respectively. Each spectra shows the absorbed energy resolved over photon energy and the relative wave-packet phase of the two states in the superposition, the blue curve shows the phase of maximal absorption. Simulations of the superposition states 3s3d and 3d4d were also conducted, the absorption spectra of 3s3d is similar to those of 2s3d and the absorption spectra of

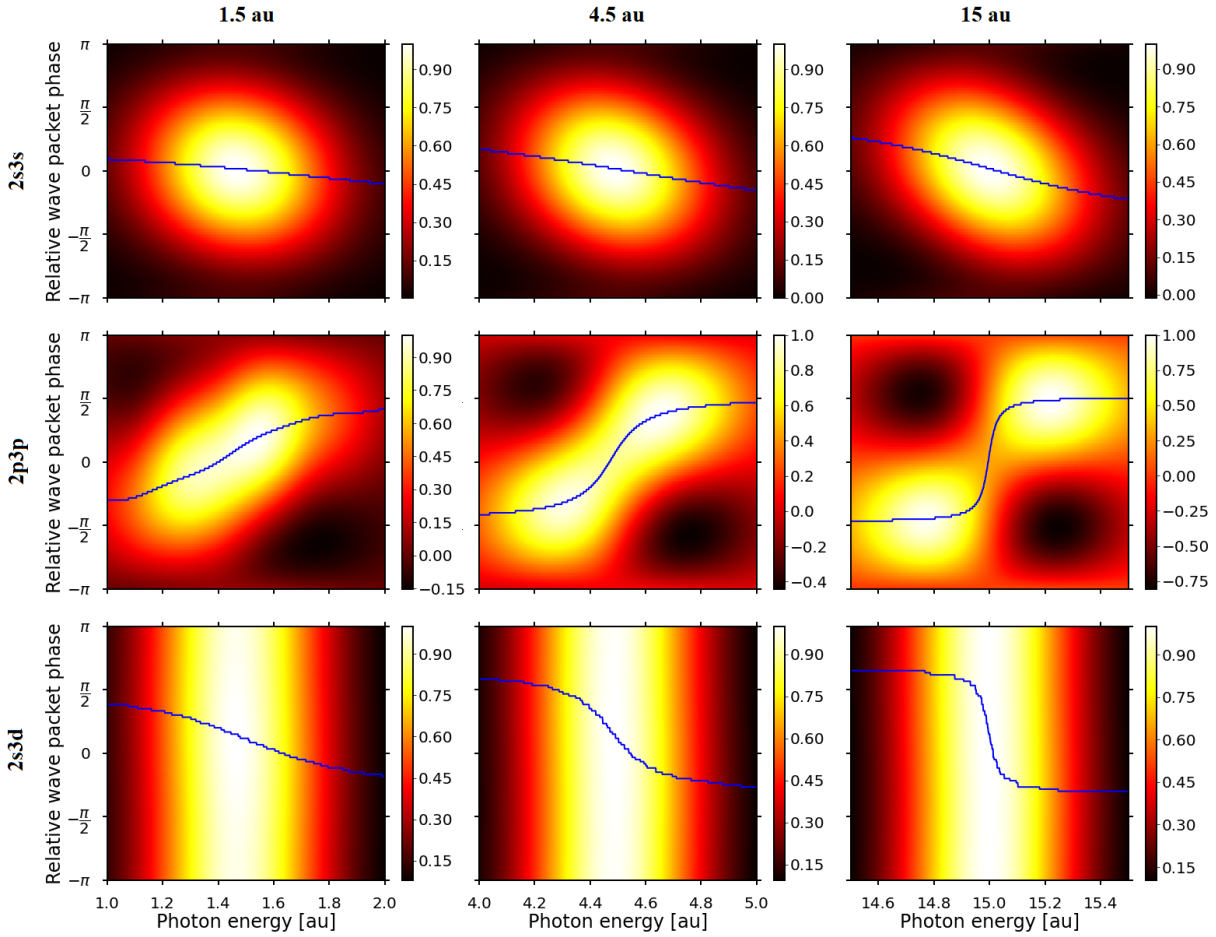

Figure 13: Attosecond transient absorption in hydrogen initially set in the superposition 2s3s, 2p3p or 2s3d (top to bottom) interacting with an attosecond pulse with central frequency 1.5 au, 4.5 au and 15 au (left to right). The absorption in arbitrary units is resolved over energy and the relative wave-packet phase of the superposition. The absorption was calculated from the observables as described in Section 2.1.3. The blue curve shows the phase of maximal absorption.

3d4d is similar to those of 2p3p. Therefore, neither of the spectra for 3s3d and 3d4d are shown here. Additionally, simulations using other pulse durations were conducted. For longer pulses similar spectra, but which were compressed in the energy dimension were observed. This is as expected as a temporally longer pulse will have a narrower frequency band [5].

Simulations of ATAS for the superposition 2s3s for a central frequency of 1.5 au have already been presented in [18]. The results in this section is a continuation of that work and investigates the behaviour of ATAS for other superpositions and central frequencies.

In the first row of Fig. 13 the absorption spectra for the superposition 2s3s in hydrogen is presented. As seen in Fig. 12, both states of the superposition are connected to the p channel in the continuum. The peak absorption is located at the central frequency of the pulse and at zero relative phase i.e. when the two states are in phase. When the states are out of phase, the absorption is diminished. An interesting feature of the absorption is that the phase of the maximum absorption varies with the photon energy, and one can see a clear tilt in the Maximal absorption phase curve. This is in

agreement with the results previously presented in [18].

In the second row of Fig. 13 the absorption for the superposition 2p3p in hydrogen is presented. Both states are connected to both the s and d channels in the continuum. In the leftmost spectra, which is simulated for the central frequency 1.5 au the absorption has a maximum as the two states are in phase and is reduced as they are taken out of phase, as in the case of the previously discussed results. However, in this case the observed tilt is in the opposite direction. One can also see some slight emission for negative phase and an energy above the central frequency. In the middle and the rightmost maps the central frequencies of 4.5 au and 15 au in hydrogen is presented. From these results it is clear that with increased central frequency the shape of the absorption goes from having one central peak to instead having four poles around the phases $\pi/2$ and $-\pi/2$. Two of these poles are absorbing and two are emitting light. This is an interesting behaviour which has not been reported previously. With increased central frequency the amplitude of the emission increases compared with the absorption and the slope of the maximum absorption phase becomes steeper at the central frequency. This behaviour will be investigated further in future work.

In the third row of Fig. 13 the absorption for the superposition 2s3d in hydrogen is presented. One can see that the absorption is mostly phase independent, although a weak phase dependence can still be seen by looking at the maximum absorption phase curve. A possible reason for this might be that in addition to the p channel, which both states share, the 3d state has an additional f channel. The excitation through this channel will not interact with the excitation from the 2s state and is therefore not phase dependent. The tilt of the maximum absorption curve is in the same direction as the 2s3s case and the opposite direction as the 2p3p case. The maximum absorption of the 2s3d is shifted slightly towards positive phases.

4.1.3 Radiation Emitted by Probed Hydrogen Atom in Superposition

In this section, the analysed reaction is H* + γ_{probe} $\rightarrow$ H*′ + γ_{rad}. It is simulated in order to investigate the energy radiated from the atom. It was found that the absorbed

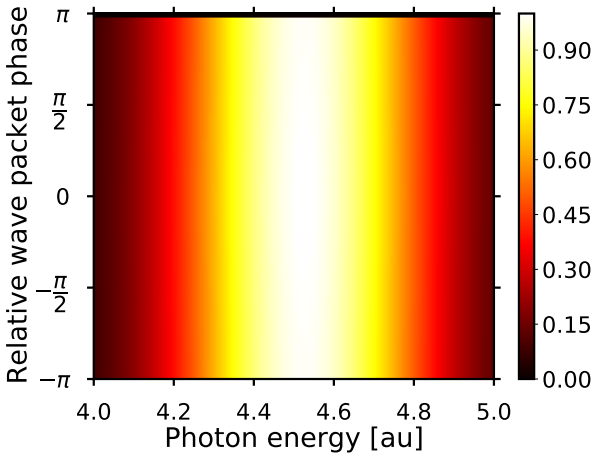

Figure 14: Energy radiated by a hydrogen atom initially set in the superposition 2s3s interacting with an attosecond pulse with the central frequency 4.5 au. The radiated energy, in arbitrary units, is resolved over photon energy and the relative wave-packet phase of the superposition. The energy was calculated as described in Section 2.1.4.

energy is larger than the radiated energy.

In Fig. 14 the radiated energy in arbitrary units is presented as a function of photon energy and relative wave-packet phase. It is simulated for a hydrogen atom in the superposition state 2s3s interacting with an attosecond pulse with a central frequency of 4.5 au. The initial wave-packet phase was scanned as described in the previous section. This spectrum is very similar to those simulated for other superposition states and central frequencies. In contrast to the ATAS results the radiated energy does not have a clear dependence on the relative wave-packet phase. The different behaviour of the absorption and radiation processes is one of the main result of this master thesis, and it will be the subject of further detailed investigations, both in and beyond the hydrogen case.

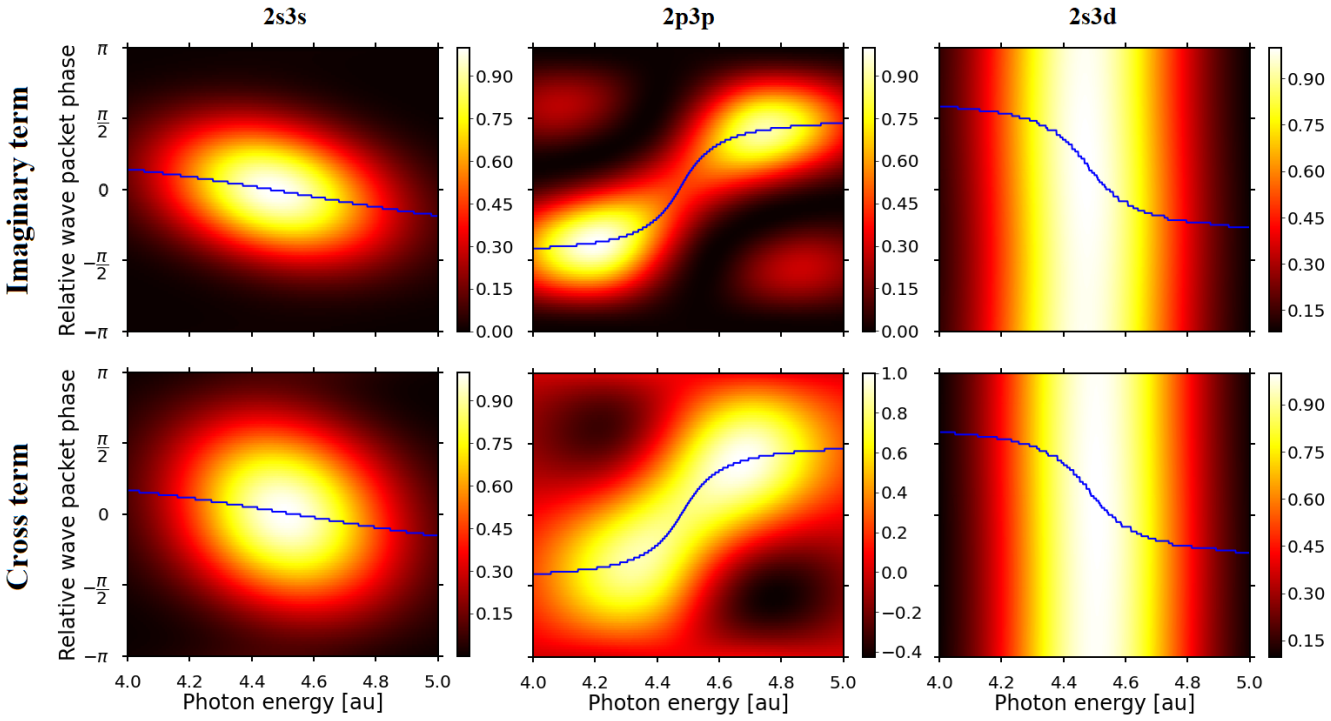

Figure 15: Energy, calculated from the imaginary part of the acceleration (first row) and the cross term, real multiplied with imaginary part of the acceleration (second row), radiated by a hydrogen atom initially set in the superposition 2s3s, 2p3p or 2s3d (left to right) interacting with an attosecond pulse with the central frequency 4.5 au. The radiated energy, in arbitrary units, is resolved over photon energy and the relative wave-packet phase of the superposition. The emitted energy was calculated from the observables as described in Section 2.1.4. The blue curve shows the phase of maximal radiation.

The radiated energy was calculated from the absolute square of the Fourier transformed acceleration expectation value. The absolute square can be divided up into the real and imaginary parts $|\widetilde{a}(\omega)|^2 = \mathrm{Re}\{\widetilde{a}(\omega)\}^2 + \mathrm{Im}\{\widetilde{a}(\omega)\}^2$. It is found that the imaginary part of the absolute value, $\mathrm{Im}\{\widetilde{a}(\omega)\}^2$, is approximately four orders of magnitude smaller than the real part. By separating the real and imaginary parts one can calculate the contribution of the imaginary part of the field to the radiated energy. In the first row of Fig. 15 the imaginary parts of the absorbed energy is presented. In the second row of Fig. 15 the cross term, the real part of the acceleration multiplied

with the imaginary part of the acceleration $\mathrm{Re}\{\widetilde{a}(\omega)\}\,\mathrm{Im}\{\widetilde{a}(\omega)\}$, is presented. It was simulated for a hydrogen atom in the initial superpositions 2s3s, 2p3p and 2s3d, in the left, middle and right panel respectively, interacting with an attosecond pulse with the central frequency 4.5 au.

One can compare the results of the imaginary and cross term of the in Fig. 15 with the corresponding ATAS results in the middle column of Fig. 13. From the first row of Fig. 15, it is clear that the dependence on the relative wave-packet phase of the radiated energy is retained in the imaginary part of the field, but that it is many times weaker than the real part which is phase independent. The shapes of the imaginary contribution spectra is similar to the ATAS results, however as the square of the imaginary part is taken no negative values are observed. The 2s3s peak is also sharper than in the case of ATAS. As in the case with the ATAS results, the tilts of the maximum absorption phase becomes larger for larger energies (not shown) and the four poles in the 2p3p results become more pronounced. The results for the cross term $\mathrm{Re}\{\widetilde{a}(\omega)\}\,\mathrm{Im}\{\widetilde{a}(\omega)\}$ in the second row of Fig. 15 are almost indistinguishable from the ATAS results. Thus, providing an interesting link between the two processes. It is not unreasonable that the profile of the energy absorbed by the atom and the energy radiated by the atom should be similar. From Fig. 15 it is clear that the dependence on relative wave-packet phase is retained in the emitted radiation. It can be noted that this is not the same phenomenon as stimulated emission as the atom is not returned to its ground state. Rather, it is the radiation induced by the exchange of high energy photons with the atom. The behaviour of the imaginary part and the cross term of the radiation spectra will be investigated further in future work.

4.2 Two-Atom Model

The two-atom model investigates the effect of coupling an atom in the ground state or a Rydberg state to an atom in a superposition state. This differs from the previous results as the perturbation is induced through the interaction between the atoms rather than from an external field. The interaction is modeled through either dipole-dipole interaction which couples the two atoms through Förster resonance energy transfer or through radiation field interaction.

The states of the two atoms are denoted $\mathcal{A}(t) \equiv (A_1(t); A_2(t))$, where $A_i(t)$ is the state of atom i at time t, $A_i(t) = (c_{1s}^{(A_i)}(t), \cdots, c_{nl}^{(A_i)}(t), \cdots)$. The shorthand $A_i(t) = nl + n'l' = (0, \cdots, c_{nl}^{(A_i)}(t) = 0.5, \cdots, c_{n'l'}^{(A_i)}(t) = 0.5, \cdots)$ is used, all superpositions are evenly populated. It was found that unevenly populated superpositions show the same behaviour but with weaker interaction, in order to get the largest interaction and therefore the fastest dynamics, evenly populated superpositions were used as an idealised case. Note that the complex state amplitude vector $\mathcal{A}(t)$ is not to be confused with the vector potential $A(t)$.

These are the parameters for all two-atom model simulations except where noted. The interaction was modeled in length gauge. The B-spline basis, described in Section 3.1.3, was defined with the following number of knot points in the different regions: $n_{inner} = 2$, $n_{linear} = 200$ and $n_{ECS} = 50$, the linear spacing $dR_{linear} = 0.5$ au, the polynomial order $k_s = 8$ and without exterior complex scaling (ECS). ECS was not used as the interaction between the atoms is weak enough that the probability of electrons being ionised is small, thus making the reflections from the edge of the simulation box negligible. Not using ECS makes the Hamiltonian hermitian. The maximum

l quantum number for the excited electrons was $l_{max} = 6$ and the maximum energy of the CIS states was $\epsilon_{max} = 8$ au. Time was discretized with a step size of 0.01 au.

4.2.1 Two Coupled Hydrogen Atoms

In this section two hydrogen atoms are coupled. An atom in a dipole allowed superposition, where the states have a l quantum number difference of $\Delta l = 1$, oscillate generating non-zero position and acceleration expectation values. This induces interaction with other atoms through dipole-dipole or radiation interaction, allowing for coupling of atoms.

In Fig. 16 a long simulation showing the evolution of the atomic states is presented. The state populations of two hydrogen atoms separated by a distance of 20 au in the initial states $\mathcal{A}(0) = (1s; 1s + 2p)$ coupled by dipole-dipole interaction is presented as 1 subtracted by the 1s population and the 2p population of atom one in blue and red (initially 0) and atom two in green and yellow (initially 0.5). The 1 - 1s and 2p population overlap, hence all population lost by the 1s state is excited to the 2p state, this is reasonable as the 1s-2p transition is resonant. The population of atom one oscillates from its initial state in 1s to the same superposition that atom two was initially in and back again, atom two does the opposite oscillation. Hence, all population in the atoms oscillates between the initial state in atom one and the initial superposition in atom two with a period time of approximately $6.2 \cdot 10^4$ au ≈ 1.5 ps. A small discrepancy is seen for large time as the total excited population at the end of the simulation is larger

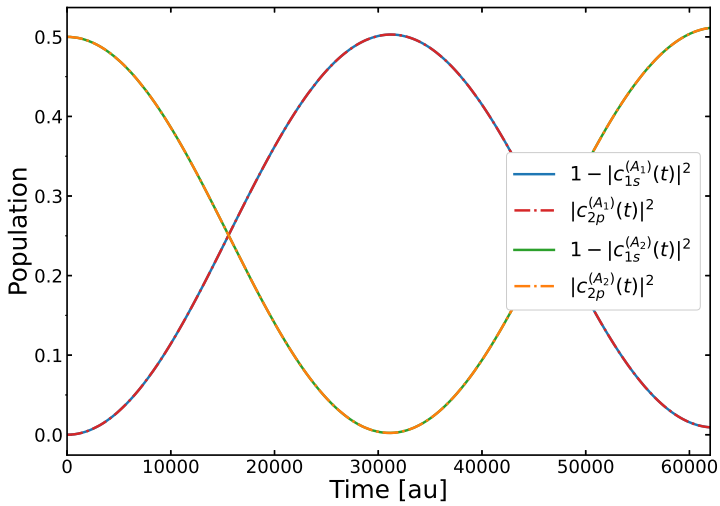

Figure 16: Populations of the 1s and 2p levels in the two atoms resolved over time. It shows the populations of the two atoms oscillate a full period over a long time. The initial setup is $\mathcal{A}(0) = (1s; 1s + 2p)$. The two atoms are coupled through dipole-dipole interaction and are separated by a distance of 20 au. The period time of the poulation oscillation is approximately $6.2 \cdot 10^4$ au ≈ 1.5 ps.

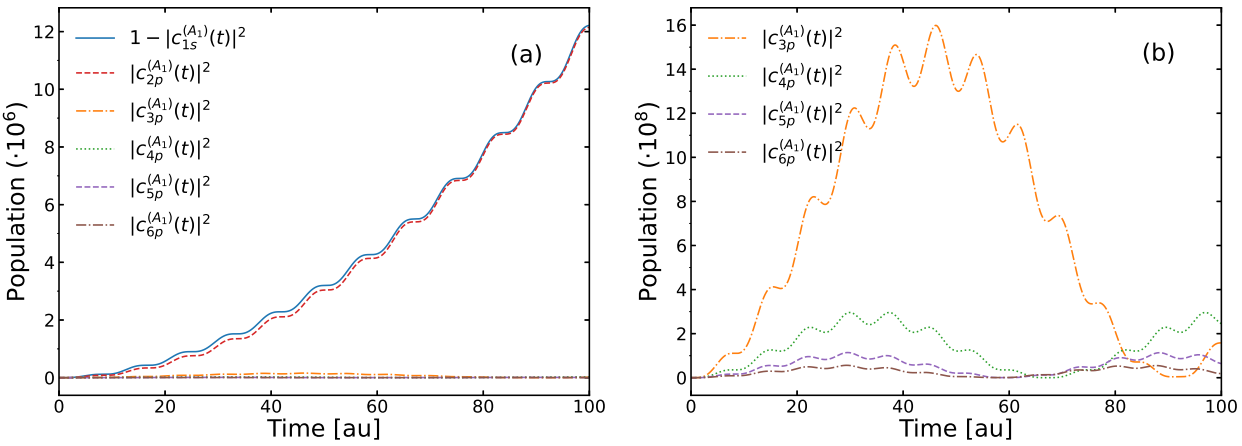

Figure 17: Populations of different states in atom one. The initial configuration is $\mathcal{A}(0) = (1s; 1s + 2p)$, the two atoms are separated by 20 au and are coupled through dipole-dipole interaction. In (a) the blue line is the difference of the 1s population from one and is therefore the sum of the excited population. Most of the population is transferred to the 2p state as the transition is resonant. In (b) the other p state are shown in order to see the population dynamics of the non-resonant states.

than at the beginning of the simulation. This is not a physical effect, rather it is an error accumulated over the large run time.

In Fig. 17 the population of several states in atom one is presented. The same simulation parameters were used as for the previous results. In (a) the $1 - 1s$ population is compared with the p state populations up to $n = 6$ quantum number. $1 - 1s$ is the total population transferred to excited levels, as seen most, but not all of, the population is transferred to the 2p level. In (b) the p states for $n \in [3, 6]$ are presented. The populations oscillate with different period time for the different states. The lower n states have larger populations and longer period times. The population of the non-p states are 5 orders of magnitude smaller than the p states population and are not shown. Through using the TDCIS method one can investigate the evolution of many atomic states, this would not be possible if one instead used a simpler model where only two states in the atom were simulated.

In Fig. 18 a comparison between the strengths of the two interactions is presented. It shows two hydrogen atoms, coupled with dipole-dipole interaction (blue line) or radiation interaction (red dashed line), simulated for several separation distances. The simulation time was 1100 au. The maximum position expectation value in atom one is resolved over distance between the two hydrogen atoms. In (a) the initial states of the atoms are $\mathcal{A}(0) = (1s; 1s + 2p)$ and in (b) the initial states are $\mathcal{A}(0) = (2s; 2s + 3p)$. The maximum dipole value in atom one, the atom which is initially not in a superposition, is used as a measure of the strength of the interaction as the dipole increases linearly with time as the atom is excited. Thus, one can determine in which domains the dipole-dipole and the radiation interaction is dominant. The point where both interactions are equally strong is the critical distance R_c.

The critical distance separating the two domains where the two interactions are equally strong can be approximated by setting the dipole-dipole and the radiation interaction to be equal. By approximating the acceleration along the z-direction as

$$a(t) = \ddot{z}(t) \approx -\omega^2 z(t), \tag{72}$$

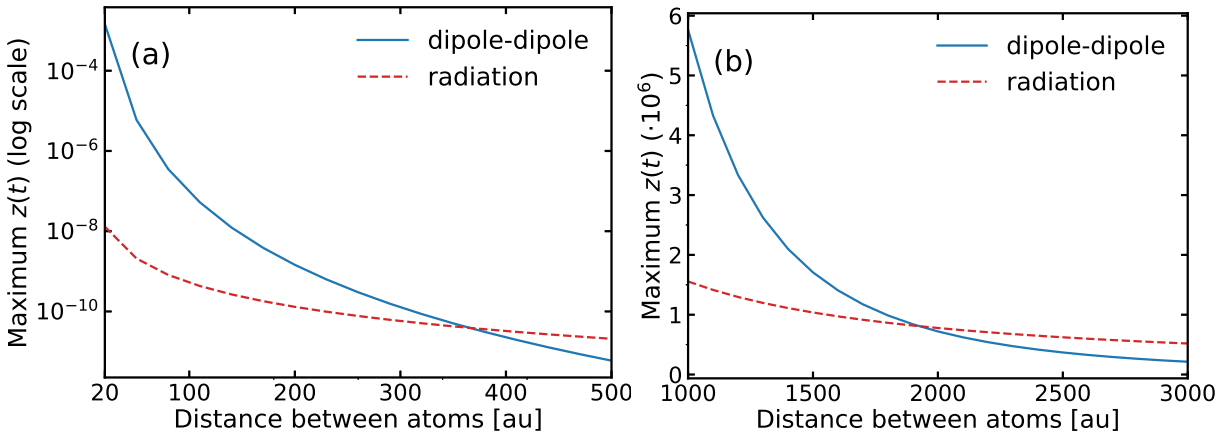

Figure 18: A comparison of the strengths of the interactions. The maximum position expectation value is used as a measure of the interaction strenght as described below. The maximum position expectation value in atom one is plotted as a function of the separation distance between two atoms coupled with dipole-dipole interaction or radiation interaction. The simulation time was 1100 au. In (a) the initial configuration was $\mathcal{A}(0) = (1s; 1s + 2p)$ and in (b) it was $\mathcal{A}(0) = (2s; 2s + 3p)$.

the critical distance becomes

$$R_c \approx \frac{c}{\omega}. \tag{73}$$

This analytical value can be compared to the results presented in Fig. 18. In (a) the critical distance is approximately 350 au, using Eq. (73) one gets the value $R_c \approx 365$ au. In (b) the critical distance is approximately 2000 au, using Eq. (73) one gets the value $R_c \approx 1970$ au. Thus, one can draw the conclusion that Eq. (73) can be used to estimate the critical distance and therefore the different domains in which the interactions are dominant.

A large increase in the critical distance is observed for the increased principal quantum number. The scaling of the critical distance for superpositions of neighbouring energy levels can be calculated by determining the dependence of the principal quantum number on the energy difference between neighbouring energy levels. The energy difference between two neighbouring energy levels in the hydrogen atom in terms of the principal quantum numbers n and $n + 1$ as

$$\omega_{n,n+1} = \frac{1}{2}\frac{1}{n^2} - \frac{1}{2}\frac{1}{(n+1)^2}, \tag{74}$$

note that the energies of the states are negative but here the energy difference is calculated which is a positive quantity. Using the average principal quantum number $n_a = (n + (n + 1))/2$ the energy difference can be approximated as

$$\omega_{n_a} = \frac{1}{2}\left(\frac{1}{(n_a - 0.5)^2} - \frac{1}{(n_a + 0.5)^2}\right) \approx \frac{1}{2}\left(\frac{1}{n_a^2} - \frac{1}{n_a^3} - \frac{1}{n_a^2} - \frac{1}{n_a^3}\right) = \frac{1}{n_a^3}, \tag{75}$$

where the approximation $f(x + dx) \approx f(x) + f'(x)dx$ has been used.

The critical distance of a superposition of neighbouring energy levels in hydrogen can thus be described in terms of the average principal quantum number by combining Eqs. (73) and (75), yielding the following expression

$$R_c \approx c n_a^3. \tag{76}$$

If one compares this expression with the results presented in Fig. 18 by setting n_a to the average of the two levels one gets $R_c \approx 460$ au for the superposition 1s2p in (a) and $R_c \approx 2140$ au for the superposition 2s3p in (b). Thus one can draw the conclusion that Eq. (76) can be used to give a rough approximation of the critical distance. It is clear that the dipole-dipole interaction is highly dependent on the principal quantum number and increases substantially, both in strength and range, for increased principal quantum numbers.

In the case of cold atoms interacting with an on-resonance laser pulse with narrow bandwidth, the atom first excited by the pulse will interact through dipole-dipole interaction with the surrounding atoms, shifting their energy levels off resonance, blockading them from excitation. This is the dipole blockade phenomenon. As is observed in the presented results the range of this dipole blockade is dependent on the excitation. Outside of this range other atoms will be excited and cause their own dipole blockades. Thus, the sample will be separated into several regions each with only one excited atom. This is an interesting phenomenon in cold atomic gases [12].

In order to relate the simulated domains to attosecond experiments one has to determine a relation between the interatomic distance to the pressure and density of the sample gas. Assuming low density, the pressure of a dilute gas of atoms will follow the ideal gas law

$$pV = Nk_BT, \tag{77}$$

where p, V, N, k_B and T is the pressure, volume, number of atoms, Boltzman constant and temperature respectively. The internal structure of the atoms will have an effect on the energy and the entropy of the gas but not the pressure [26].

Assuming the gas to be locally uniform the density is $\rho = N/V$ and each atom approximately occupies the volume $V/N \approx d^3$, where d is the atomic distance, one arrives at following relations for the density and the pressure

$$\begin{aligned} \rho &= \frac{1}{d^3} \\ p &= \frac{1}{k_B T d^3}. \end{aligned} \tag{78}$$

In a typical HHG experiment the pressure is around 1 mbar to 10 mbar and the temperature is around room temperature ($T \approx 300$ K). In a freely expanding jet the pressure is not measured, however it is known that the typical density is $\rho \approx 10^{19}$ m^{-3} [27].

Using the relations in Eq. (78) one arrives at the following atomic distances. For a HHG experiment the distance between the atoms is between the distances 300 au and 700 au, this is around the critical distance for the superposition 1s2p and in the dipole-dipole domain for the 2s3p superposition. For the case of the freely expanding jet the atomic distance is approximately 10^4 au, this is in the radiation domain for the presented results. Using the expression for the scaling of R_c, in Eq. (76), one can predict that it will be in the dipole-dipole domain for the superposition 4s5p and higher principal quantum numbers. It has to be noted that the calculated distances are the distance between the nearest atoms. It could therefore be that an atom in a sample affects the atoms in its vicinity by dipole-dipole interaction and the atoms farther away with radiation interaction. Due to the scaling, dipole-dipole interaction can have very large domains if the atom is excited to high principal quantum numbers. This model could be compared to cold atom experiments on the dipole-blockade in order to investigate the range of the dipole-dipole domain.

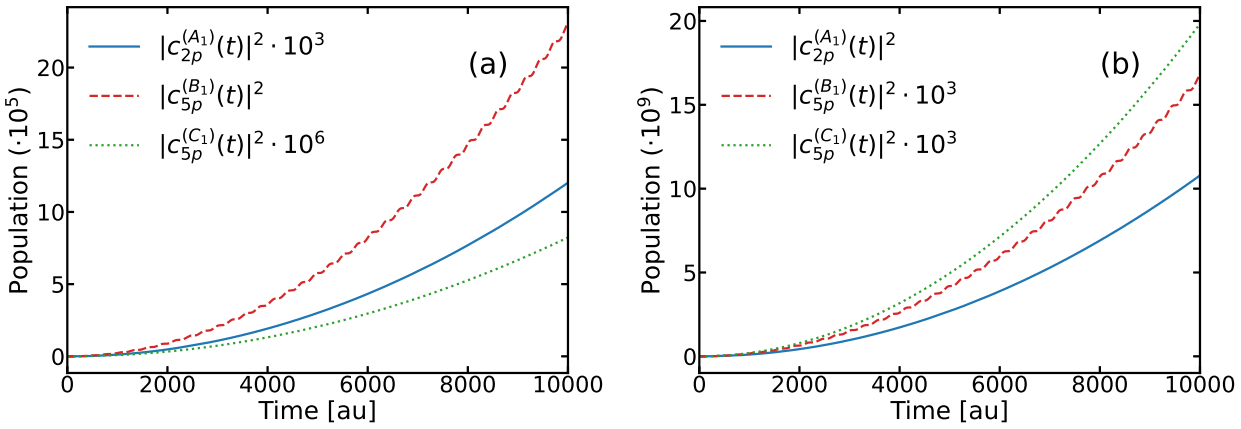

Figure 19: A comparison of the population of the resonant transition in atom one for the three initial configurations $\mathcal{A}(0) = (1s; 1s + 2p)$, $\mathcal{B}(0) = (4s; 4s + 5p)$ and $\mathcal{C}(0) = (1s; 1s + 5p)$. The distance between the atoms is 200 au. The atoms are coupled by dipole-dipole interaction in (a) and by radiation interaction in (b). Note the multiplicative factors in the legend.

In Fig. 19 simulations of two hydrogen atoms separated by 200 au coupled by dipole-dipole interaction in (a) and by radiation interaction in (b) for different state setups are presented. The state setups are $\mathcal{A}(0) = (1s; 1s + 2p)$, $\mathcal{B}(0) = (4s; 4s + 5p)$ and $\mathcal{C}(0) = (1s; 1s + 5p)$. For the dipole-dipole interaction in (a) the final population of setup $\mathcal{B}$ is three orders of magnitude larger than setup $\mathcal{A}$ whilst for setup $\mathcal{C}$ it is three orders of magnitude smaller than $\mathcal{A}$. For the radiation interaction in (b), the final populations of setups $\mathcal{B}$ and $\mathcal{C}$ are both three orders of magnitude smaller than setup $\mathcal{A}$.

In order to verify the numerical approach and its implementation with analytical values, one can construct an analytical two level model since the excitation to other levels is small as seen in Fig. 17. This analytical model can predict the numerical model for small times using a perturbation theory approach. This is done through following the work presented in chapter 7 of [16]. The two level wave function is defined as

$$|\Psi(t)\rangle = c_1(t)\,|1\rangle\, e^{-i\omega_1 t} + c_2(t)\,|2\rangle\, e^{-i\omega_2 t}. \tag{79}$$

where c_i, ω_i and $|i\rangle$ is the state amplitude, energy and time independent wave function of state i respectively. From the wave function the expectation value of the position in atom two can be approximated as

$$z_2(t) = c_1^*(t)c_2(t)\,\langle 1|\,\hat{z}\,|2\rangle\,(\cos(\omega_{21}t) - i\sin(\omega_{21}t)) + c.c. \approx \langle 1|\,\hat{z}\,|2\rangle\cos(\omega_{21}t), \tag{80}$$

where $\langle 1|\,\hat{z}\,|2\rangle$ is real as it is an observable, $\omega_{21} = \omega_2 - \omega_1$ is the resonant energy of the superposition state. For small times the population change in atom two is small, and thus the state amplitudes can be approximated by the real value $c_1(t) = c_2(t) = c_1(0) = 2^{-1/2}$ as they are equally populated.

Using the relation in Eq. (72) the two potentials can be written on the general form

$$\hat{V}(\tau) = K\,\langle 1|\,\hat{z}\,|2\rangle\,\hat{z}\cos(\omega_{21}t) \tag{81}$$

where $K = R^{-3}$ for dipole-dipole interaction and $K = -\omega_{21}^2 c^{-2} R^{-3}$ for radiation interaction.

Inserting the two level wave function into the TDSE Eq. (1) one arrives at the following equations of motion

$$\begin{aligned} i\dot{c}_1 &= \Omega \cos(\omega t) e^{-i\omega_{21}t} c_2, \\ i\dot{c}_2 &= \Omega^* \cos(\omega t) e^{i\omega_{21}t} c_1. \end{aligned} \tag{82}$$

Where $\Omega = \langle 1| K \langle 1| \hat{z} |2\rangle \hat{z} |2\rangle = K z_2 \langle 1| \hat{z} |2\rangle^2$ is the Rabi frequency. As the population of atom one is initially in the lower state $c_1(0) = 1$ and $c_2(0) = 0$. Integrating the equations of motion and applying the rotating wave approximation one arrives at the following expression for the population of state two

$$\begin{aligned} |c_2(t)|^2 &= \left| \Omega \frac{\sin((\omega_{21} - \omega)t/2)}{\omega_{21} - \omega} \right|^2 \\ &= \frac{1}{4} |\Omega|^2 t^2 \left(\frac{\sin((\omega_{21} - \omega)t/2)}{(\omega_{21} - \omega)t/2} \right)^2 \\ &\approx \frac{1}{4} K^2 \langle 1| \hat{z} |2\rangle^4 t^2, \end{aligned} \tag{83}$$

where the approximation that the population transfer is resonant, as has been observed, is used. From this expression it is clear that the population increases with the square of the time. This is in agreement with the numerical results.

The dipole transition matrix elements are calculated from the tabulated values in [28] of the square of the dipole moments multiplied with the angular part, calculated using Eq. (66). The radiation and the dipole results can be compared through dividing the two populations as

$$\frac{|c_2(t)|^2_{dip}}{|c_2(t)|^2_{rad}} = \left(\frac{c}{R\omega_{21}} \right)^4. \tag{84}$$

The comparison between the fraction of the populations, depending on the interaction, for the numerical and analytical values is seen in Table 2, showing good agreement.

Table 2: Fraction of the populations of the excited state for the two interactions, calculated as dipole-dipole divided by radiation.

	Numerical value	Analytical value
1s2p: Dipole/Radiation	11.15	11.13
1s5p: Dipole/Radiation	4.152	4.147
4s5p: Dipole/Radiation	$1.376 \cdot 10^7$	$1.375 \cdot 10^7$

The results simulated for superposition states $n_1 s n_2 p$ and $n_1' s n_2' p$ are compared through calculating the population fraction for the dipole interaction is

$$\left(\frac{|c_2(t)|^2_{n_1 n_2}}{|c_2(t)|^2_{n_1' n_2'}} \right)_{dip} = \frac{\langle n_1 s| \hat{z} |n_2 p\rangle^4}{\langle n_1' s| \hat{z} |n_2' p\rangle^4}, \tag{85}$$

and for radiation interaction it is

$$\left(\frac{|c_2(t)|^2_{n_1n_2}}{|c_2(t)|^2_{n_1'n_2'}}\right)_{rad} = \frac{\omega^4_{n_1n_2}\left\langle n_1 s\right|\hat{z}\left|n_2 p\right\rangle^4}{\omega^4_{n_1'n_2'}\left\langle n_1' s\right|\hat{z}\left|n_2' p\right\rangle^4}. \tag{86}$$

The comparison between the fraction of the populations, depending on the superposition states of the atoms, for the numerical and analytical values is seen in Table 3, showing good agreement.

Table 3: Fraction of the populations of the excited state for different superpositions simulated with dipole-dipole interaction coupling (first three rows) and radiation interaction (last three rows).

	Numerical value	Analytical value
Dipole: 1s2p/4s5p	$5.223 \cdot 10^{-4}$	$5.250 \cdot 10^{-4}$
Dipole: 1s2p/1s5p	1461	1470
Dipole: 4s5p/1s5p	$2.796 \cdot 10^{6}$	$2.796 \cdot 10^{6}$
Radiation: 1s2p/4s5p	644.8	648.2
Radiation: 1s2p/1s5p	544.2	547.6
Radiation: 4s5p/1s5p	0.8440	0.8449

4.2.2 Two Coupled Helium Atoms

In order to investigate the two-atom model for the beyond hydrogen case, simulations of two coupled helium atoms were conducted. The number of knot points in the inner region was changed to $n_{inner} = 20$ in order to better describe the helium atom.

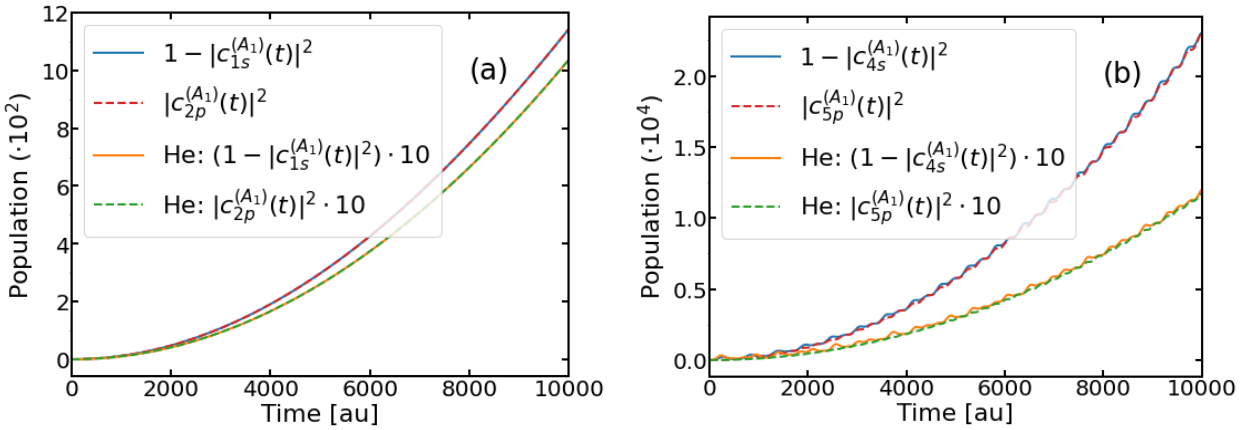

Figure 20: A comparison of the populations in atom one for two coupled hydrogen atoms and two coupled helium atoms. The coupling was modelled with dipole-dipole interaction. The initial state setup was $\mathcal{A}(0) = (1s; 1s + 2p)$ with a separation distance of 20 au in (a) and $\mathcal{A}(0) = (4s; 4s + 5p)$ with a separation distance of 200 au in (b). Note the multiplicative factors in the legend.

In Fig. 20 the population in atom one is compared between two coupled hydrogen atoms and two coupled helium atoms for the initial superposition $\mathcal{A}(0) = (1s; 1s + 2p)$ for the separation distance 20 au in (a) and $\mathcal{A}(0) = (4s; 4s + 5p)$ for the separation distance in (b). As observed for both cases the population of the upper state is an order of magnitude smaller for the two coupled helium atoms. Otherwise, the behaviour is similar for both atom types.

The populations in hydrogen and helium can be compared using Eq. (85). The z-component of the position expectation value in helium was calculated from the tabulated values of the oscillator strengths in [29]. The expectation values are smaller for helium than hydrogen. The comparison between the numerical and analytical value of the fraction of the population in hydrogen divided the population in helium is presented in Table 4. The tabulated results show agreement between the numerical and analytical models. It should be noted that the discrepancy between analytical and numerical is larger than for comparisons between hydrogen atoms, this could be a consequence of the helium atom having more than one electron and therefore not being completely described by the TDCIS method as double excitations are not taken into account. Although, as the energy transfer in the two-atom model is mostly resonant, I would expect that the restriction of only having single excitations should have a small effect on the results of the many-electron atoms.

Table 4: Fraction of the populations of the excited state for simulations of two atoms of the same type coupled by dipole-dipole interaction. The values are calculated as the final population in hydrogen divided by the final population in helium.

	Numerical value	Analytical value
1s2p: H/He	11.02	9.83
4s5p: H/He	19.67	20.52

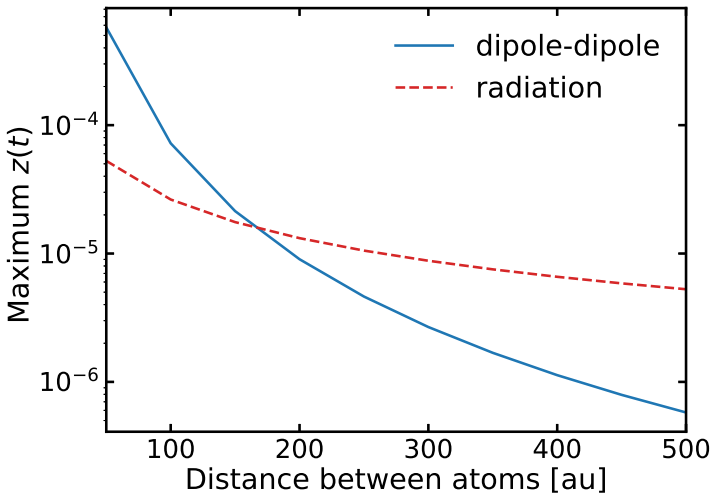

Figure 21: A comparison of the strengths of the interactions in helium. The maximum position expectation value in atom one is plotted as a function of the separation distance between two atoms coupled with dipole-dipole interaction or radiation interaction. The simulation time was 1100 au and the initial state was $\mathcal{A}(0) = (1s; 1s + 2p)$.

In Fig. 21 the strengths of the two interactions simulated in helium is presented. Two helium atoms initially in the states $\mathcal{A}(0) = (1s; 1s + 2p)$, were simulated for several separation distances. The same parameters as for Fig. 18 were used. The maximum position expectation value in atom one is resolved over distance between the two helium atoms. By comparing these results with Fig. 18 it is clear that the critical distance is smaller in the case of helium. The critical distance calculated from Eq. (73), for the energy distance between the 1s and 2p levels in helium, is $R_c \approx 172$. Comparing this with the results in Fig. 21 good agreement is found. These results show that studies of atoms beyond the hydrogen atom is possible through the TDCIS method, allowing for investigation of heavier noble gases such as neon and argon with comparable effort in future works.

4.3 Many-Atom Model

The many-atom model is used to investigate propagation effects of an attosecond pulse through a macroscopic medium. The fields in the sample are presented in Section 4.3.1. The radiation emitted by the sample and its angular distribution is presented in Section 4.3.2. The energy radiated by the sample and dissipated by propagation through the macroscopic sample is presented in Section 4.3.3.

These are the parameters for all many-atom model simulations except where noted. The interaction was modelled in length gauge. The B-spline basis, described in Section 3.1.3, was defined with the following number of knot points in the different regions: $n_{inner} = 2$, $n_{linear} = 150$ and $n_{ECS} = 40$, the linear spacing $dR_{linear} = 0.5$ au, the polynomial order $k_s = 8$ and with an exterior complex scaling angle of $\theta_{ECS} = 15°$. The maximum l quantum number for the excited electrons was $l_{max} = 8$ and the maximum energy of the CIS states was $\epsilon_{max} = 10$ au. Time was discretized in the interval -20 au to 20 au. The time step size, $\Delta t = 0.073$ au, was used. Thus, the unit volume length became $\Delta L \approx 10$ au ≈ 5 Å. The external field had the vector potential amplitude $A_0 = 0.001$ au, the central frequency $\omega_0 = 1.5$ au ≈ 40.8 eV and the pulse width $\tau_e = 5$ au ≈ 121 as.

A small macroscopic-like sample was used in order to keep the computational times reasonable and still investigate the effects of many-atom propagation. The sample length was 5000 au ≈ 2650 Å, the radius was 2000 au ≈ 1060 Å and the sample had 100 occupied unit volumes. The density used was 10^{-7} Å^{-3} which is a typical density for a HHG experiment [27].

4.3.1 Field Propagation

In Fig. 22 the external, radiation and induced fields are compared for the different propagation models. The presented fields are those affecting the unit volume in the middle of the sample. In (a) the atomic-line model is used. The atoms are placed on a line and radiate according to Eq. (26). The propagating radiation is modelled through Eq. (42). In (b) the atomic-bulk model is used. The atoms are placed uniformly on parallel sheets and radiate only in the forward direction. The radiation is modelled according to Eq. (43). As for the case of an infinite uniformly charged sheet the generated field does not diminish with distance. In both models the generated fields counteract the external field as expected. The induced field has the same magnitude in both models as it is only dependent on the unit volume in which it is generated. The radiation

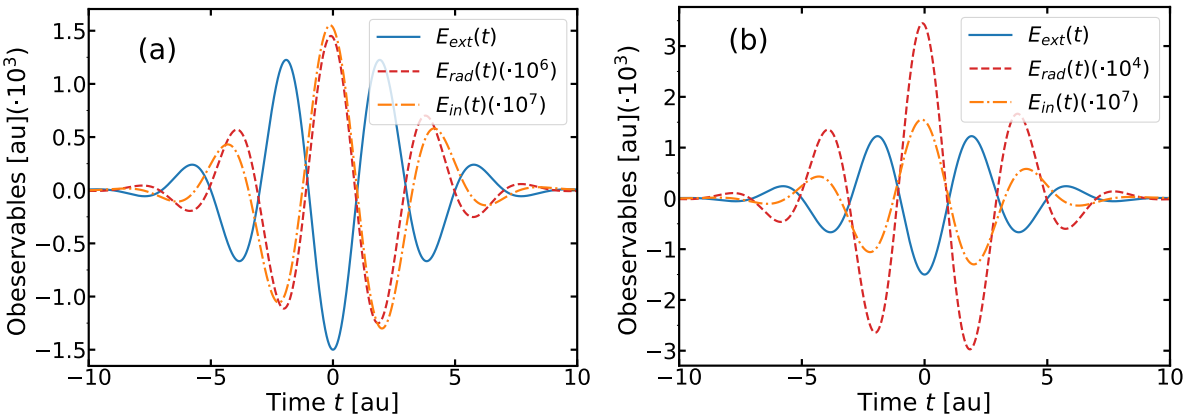

Figure 22: Comparison of fields resolved over time in the unit volume in the middle of the sample. Simulated for propagation of an attosecond pulse. In (a) atomic-line modelled was used and in (b) atomic-bulk modelled was used. Note the multiplicative factors in the legend.

field is substantially larger in (b) than in (a) and will therefore have a larger effect in the propagation of the atomic-bulk model.

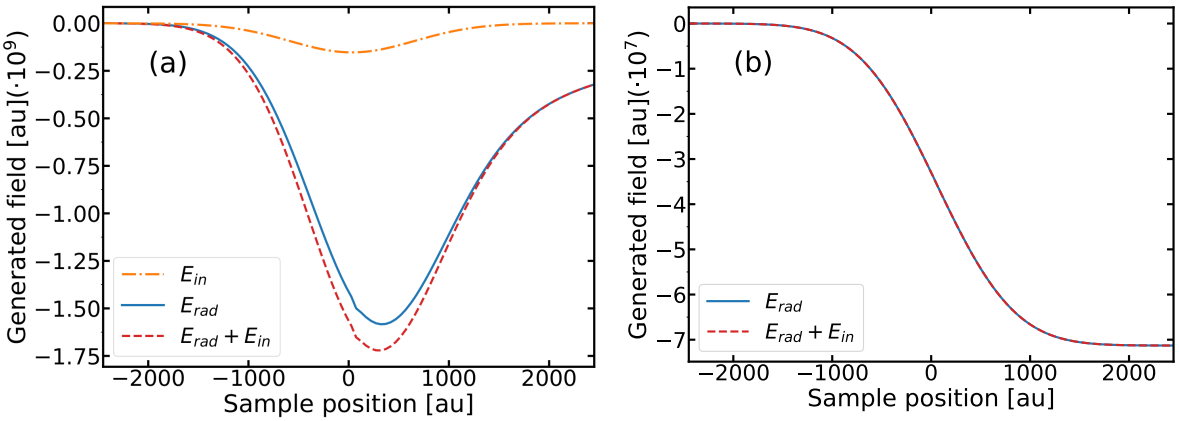

Figure 23: The maximum generated field in a unit volume resolved over its position in the sample. The curves denote the propagation used it is either, the induced field, the radiation field or both. In (a) atomic-line modeled was used and in (b) atomic-bulk modeled was used. The generated field is calculated as the difference between the total field and the external field in the unit volume. Since the propagation attenuates the incoming field, the generated field is negative.

The total field in a unit volume E_{tot} is the sum of the external field E_{ext} and the propagating fields. By taking the difference between the external field and the total field the generated field can be computed $E_{gen} = E_{tot} - E_{ext}$. It should be noted that as the total field is smaller than the external field (due to the generated field being aligned against the external field) the generated field will be negative. In Fig. 23 the maximal generated field in a unit volume is plotted against the position of said unit volume. The different curves are different propagating fields, composed of the induced field, the radiation field or both. This is done to illustrate the effect the propagation has throughout the sample. In (a) the atomic-line model is used, in (b) the atomic-bulk model is used. As seen in Fig. 22 the induced generated field is smallest (for the sim-

ulated parameters). It is proportional to the atomic density in the sample, since the atomic density is Gaussian so is the induced field. In (a) the radiation field has a peak beyond the middle of the sample. The peak is created as the radiation is accumulated from previous unit volumes and is proportional to the density and the inverse distance, placing the peak after the peak density. In (b) the radiation does not scale with distance and therefore accumulates as the external field propagates through the sample, giving an inverse exponential like behaviour. The build up of the radiation dominates the generated field, rendering the induced field negligible.This is seen in Fig. 23(b) where the generated field containing only the radiation part (blue full line) overlaps the generated field when both the radiation and induced components are taken into account (red dashed line). It is the atomic-bulk model in (b) which should be used for the investigation of the propagation of the field, whilst the atomic-line model is used to investigate the angular distribution of the generated radiation. In future work the atomic-bulk model should be compared with experiments where the absorption of a macroscopic sample is measured.

4.3.2 Radiation Emitted by a Macroscopic Sample

The radiation field emitted by the sample, detected at position $\vec{r}$, $\vec{E}_{rad}(\vec{r},t)$ is described according to Eq. (45). By rotating a detection point around the sample the angular distribution of radiation emitted by the many-atom sample can be determined. The propagation was modelled using the atomic-line model, in which the radiation generated from each atom is emitted with the angular distribution illustrated in Fig. 1.

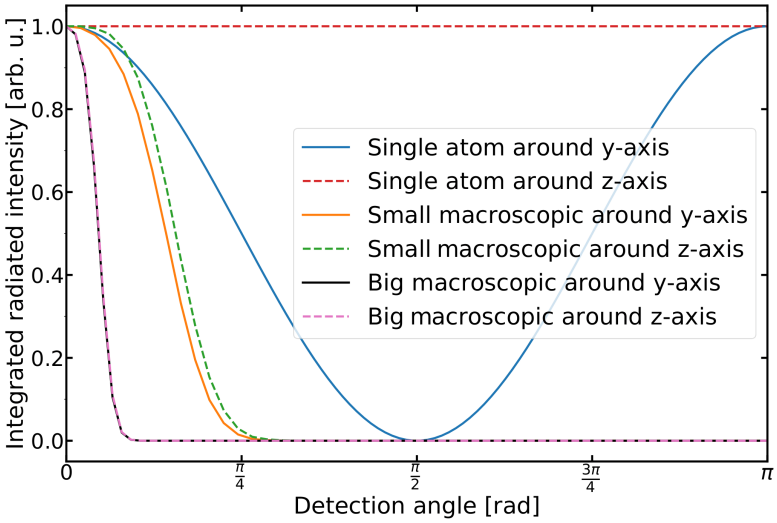

Figure 24: Integrated radiation resolved over angle rotated around the y-axis (full lines) and the z-axis (dashed lines). Detection angle zero is in the forward direction on the positive x-axis. The figure compares the radiation distribution of a single atom with the distribution of a small macroscopic sample and a larger macroscopic sample.

In Fig. 24 the normalised integrated radiated intensity, calculated as the time integrated intensity $I(t) = \vec{E}_{rad}(\vec{r},t)^2(2c)^{-1}$, is resolved over the detection angle. The detection point is set far from the sample. Zero detection angle is in the positive x-direction, i.e. the forward direction of the external field. In the figure, the radiation

distribution of a single atom is compared to the radiation of the small macroscopic sample as described above and a big macroscopic sample. The big macroscopic sample was defined with the length $L = 10^5$ au ≈ 5 μm and the radius $R = 4 \cdot 10^4$ au ≈ 2 μm. It contained 10000 unit volumes, 1000 of which were occupied. It should be noted that this sample is big in relation to the other simulated sample, but not compared to samples typically investigated in experiments. Samples on the scale of experiments can be simulated, the sample used here was chosen in order to limit the computational time.

The macroscopic radiation is emitted in the forward direction. It is observed that larger samples emits more collimated radiation. The radiation distribution of the big macroscopic sample is the same in both rotation directions. In the case of the small macroscopic sample the peak is sharper for rotation around the y-axis. This is because atoms do not radiate in the polarisation direction, *see* Fig. 1. The small macroscopic sample peak is wide enough to be affected. Because of this, the small macroscopic sample curve follows the single-atom curve for small rotation angles around the y-axis. For the big sample, the radiation seems to be symmetric with respect to rotation around the x-axis.

The main result in this section is that one can, with the use of the atomic-line model, show that larger samples generate more collimated radiation in the forward direction.

4.3.3 Macroscopic Energy Spectra

In this section, the energy dissipated in the macroscopic sample is presented. The results are resolved over photon energy and relative wave-packet phase, as described in Section 4.1.2. The results were simulated with the time step size $\Delta t = 0.01$ au. The propagation was modelled using the atomic-bulk model.

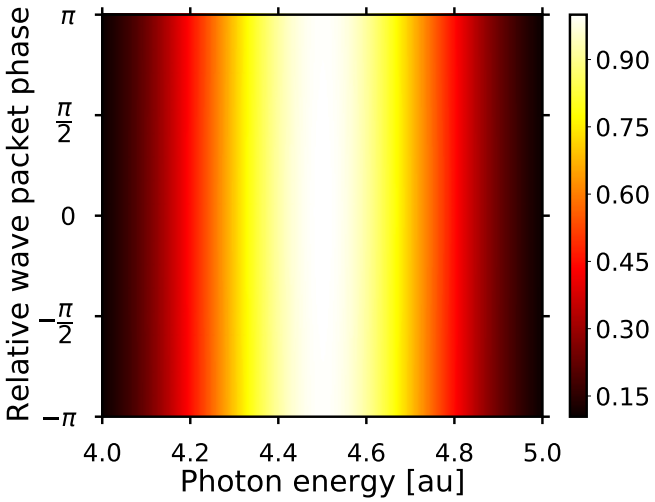

Figure 25: Spectra showing the energy dissipated in the macroscopic sample. The sample is composed of hydrogen atoms prepared in the 2s3s superposition state, interacting with an attosecond pulse with central frequency 4.5 au.

The energy dissipated in the macroscopic sample prepared in the 2s3s state, impinged on by an attosecond pulse with the central frequency 4.5 au, is presented in Fig. 25. Results for other superposition states and pulse energies are similar, and therefore not presented. The results are similar to those for the single-atom radiation

spectra, *see* Fig. 14, in that there is no visible relative wave-packet phase dependence. Again, it is found that the real part of the energy is dominant over the imaginary part.

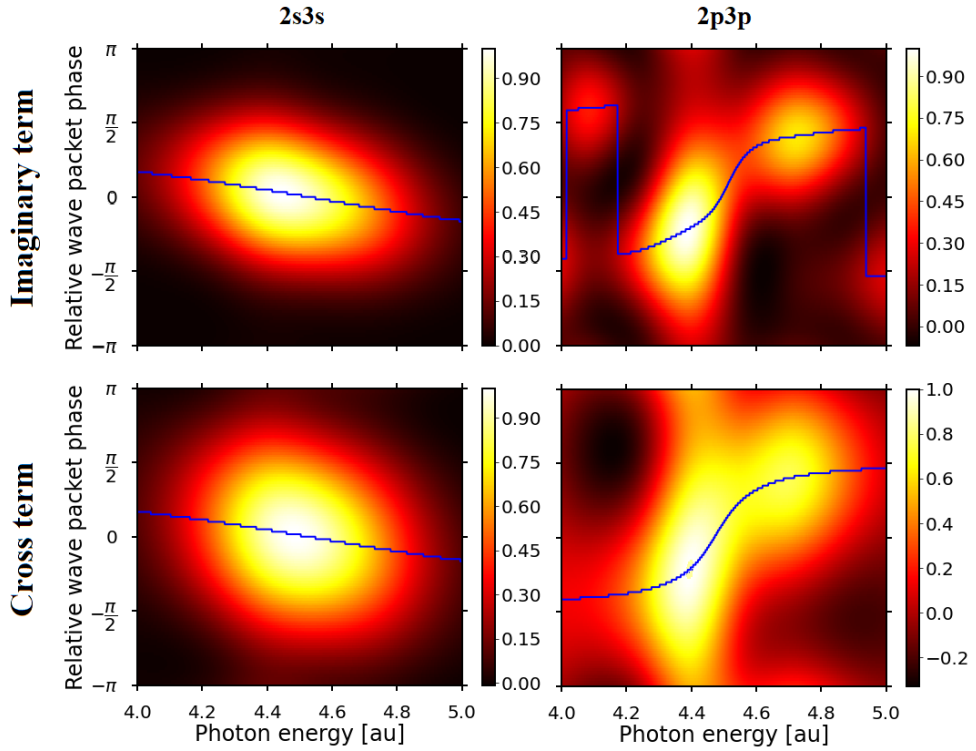

Figure 26: Spectra showing the energy dissipated in the macroscopic sample calculated from the imaginary components (first row) and the cross term, $\mathrm{Re}\{E_{abs}\}\,\mathrm{Im}\{E_{abs}\}$, (second row) of the in and out-going fields. The sample is composed of hydrogen atoms prepared in the 2s3s and 2p3p superposition state (left and right respectively), interacting with an attosecond pulse with central frequency 4.5 au.

The dissipated energy spectra for the imaginary component, $\mathrm{Im}\{E_{abs}\}^2$, and for the cross term, $\mathrm{Re}\{E_{abs}\}\,\mathrm{Im}\{E_{abs}\}$, is presented in the first and second row of Fig. 26 respectively. Hydrogen atoms, initialised in the superpositions state 2s3s (left panel) and 2p3p (right panel), were impinged upon by an attosecond pulse with central frequency 4.5 au. These results are similar to those presented in Fig. 15. It is clear that a similar dependence on the relative wave-packet phase observed in the single-atom case is retained for the many-atom case. It is not unreasonable that the propagation of the field, which is dominated by the radiation contribution, should give an energy dissipation profile which is similar to the single atom radiation profile. The propagation through the sample deforms the dissipated energy profile of the single atom. As with Fig. 15 the cross term results are closer to the single-atom ATAS results presented in the middle column of Fig. 13. The imaginary and cross-terms dependence on the relative wave-packet phase will be further investigated in future work.

5 Conclusion and Outlook

In this master thesis different aspects of light–matter interaction on the attosecond timescale have been investigated using various semi-classical approaches from the microscopic to the macroscopic regime. Three models have been studied, a single-atom model, a two-atom model and a many-atom model, each encompassing different phenomena. The models were implemented and investigated using the atomic systems of hydrogen and helium, described through the TDCIS method. Through this project the models have been constructed and tested it opens the possibility for their use in studying more complicated atomic systems. The acceleration expectation value and the constructed models will be implemented in velocity gauge as well length gauge.

Investigation of the single-atom response to attosecond pulses was conducted, yielding reasonable time-dependent expectation values. ATAS simulations were conducted validating the earlier results and expanding on them through investigation of further superpositions of different angular momenta and pulse energies. Simulated radiated energy spectra shows a largely relative wave-packet phase independent result, however the phase dependence was shown to be retained in the imaginary part of the acceleration. It was found that the profile of the cross term spectra shows good agreement with the ATAS results. This will be investigated further in future work.

The constructed two-atom model allowed for the study of the interaction between atoms. The Förster resonant energy transfer phenomenon was used as validation of the approach. Dipole-dipole interaction was compared to radiation interaction, showing distinct domains in which the interactions are dominant. The domains were compared to the macroscopic properties of pressure and density of typical attosecond experiments. As the whole electronic spectrum was used, effects of the non-resonant levels were observed. The dependence of atomic separation and initial states was investigated, analytical models were constructed in order to compare with the numerical results showing good agreement. Helium systems were compared to the hydrogen systems showing similar, but weaker dipole-dipole interaction strengths. A natural development of the two-atom model would be to add more atoms and to investigate the dynamics depending on the initial states and separation distances of the atoms. As the atoms are simulated in parallel, adding more atoms will not make the model much more numerically expensive than a single-atom simulation. Collective coherent effects are very sensitive to these parameters and can be further probed by external fields. Additional interesting applications are ionisation from inter-atomic interaction and the investigation of the dipole-blockade effect in cold-atom physics.

The many-atom model allowed for propagation of an external field through a non-uniform sample where macroscopic polarisation and radiation was taken into account. The two different geometries analysed, different aspects of macroscopic light–matter interaction. The atomic-line model was used to investigate the angular distribution of the generated radiation field, showing that longer samples generate more collimated radiation in the forward direction. The atomic-bulk model showed inverse-exponential like attenuation of the field. As with the single-atom response the wave-packet phase dependence is retained in the imaginary part and cross term of the dissipated field. The profile of the dissipated energy was found to be slightly deformed due to the propagation through the bulk of atoms. The characteristics of the imaginary part and the cross term of the energy dissipated in macroscopic samples will be investigated further in future work.

These models lead the way for further studies of the inter-atomic and collective effects of many-atom light–matter interaction between atoms and attosecond pulses.

Acknowledgements

I would like to thank my supervisors Felipe Zapata and Marcus Dahlström for their supervision, as well as the entire theoretical light-matter dynamics group for interesting discussion throughout this project. Additionally, I would like to thank Per Eng-Johanson for his insight into the experimental aspects of attosecond physics.

Appendices

A Derivation of Observable Operators

The commutator in the velocity operator derivation given in Eq. (10) is solved as follows:

$$\begin{aligned}
-\frac{i}{2}\sum_{j=1}^{N}[\hat{z},\hat{p}_j^2]f &= \frac{i}{2}\sum_{j=1}^{N}\left(\sum_{i=1}^{N} z_i\nabla_j^2 f - \nabla_j^2\sum_{i=1}^{N} z_i f\right) \\
&= \frac{i}{2}\sum_{j=1}^{N}\left(z_j\nabla_j^2 f - \nabla_j^2 z_j f\right) \\
&= \frac{i}{2}\sum_{j=1}^{N}\left(z_j\nabla_j^2 f - z_j\nabla_j^2 f - f\nabla_j^2 z_j - 2\nabla_j z_j\nabla_j f\right) \\
&= \sum_{j=1}^{N} -i\hat{\epsilon}_z\nabla_j f \\
&= \sum_{j=1}^{N} -i\frac{\partial}{\partial z_j}f, \\
\hat{v}_z &= \sum_{i=1}^{N}\hat{p}_{z_i},
\end{aligned} \tag{87}$$

where the momentum operator, $\hat{p}_j = -i\nabla_j$, acts on electron j and f is a test function, which is dependent on the coordinates of all electrons.

The acceleration operator given in Eq. (14) contains three terms containing commutators, these are solved separately. The first term becomes

$$\begin{aligned}
iZ\sum_{j=1}^{N}\left[\hat{v}_z,\frac{1}{r_j}\right]f &= Z\sum_{j=1}^{N}\left(\sum_{i}^{N}\frac{\partial}{\partial z_i}\frac{1}{r_j}f - \frac{1}{r_j}\sum_{i}^{N}\frac{\partial}{\partial z_i}f\right) \\
&= Z\sum_{j=1}^{N}\left(\frac{\partial}{\partial z_j}\frac{1}{r_j}f - \frac{1}{r_j}\frac{\partial}{\partial z_j}f\right) \\
&= Z\sum_{j=1}^{N}\left(f\frac{\partial}{\partial z_j}\frac{1}{r_j} + \frac{1}{r_j}\frac{\partial}{\partial z_j}f - \frac{1}{r_j}\frac{\partial}{\partial z_j}f\right) \\
&= -Z\sum_{j=1}^{N} f\frac{z_j}{r_j^3}.
\end{aligned} \tag{88}$$

The second term becomes

$$\begin{aligned} iE(t)\sum_{j=1}^{N}[\hat{v}_z, z_j]f &= -E(t)\sum_{j=1}^{N}\left(\sum_i^N \frac{\partial}{\partial z_i} z_j f - z_j \sum_i^N \frac{\partial}{\partial z_i} f\right) \\ &= -E(t)\sum_{j=1}^{N}\left(\frac{\partial}{\partial z_j} z_j f - z_j \frac{\partial}{\partial z_j} f\right) \\ &= -E(t)\sum_{j=1}^{N}\left(f + z_j \frac{\partial}{\partial z_j} f - z_j \frac{\partial}{\partial z_j} f\right) \\ &= -E(t)\sum_{j=1}^{N} f \\ &= -fNE(t). \end{aligned} \tag{89}$$

The third term becomes

$$\begin{aligned} -i\sum_{j>k}^{N}\left[\hat{v}_z, \frac{1}{|\vec{r}_j - \vec{r}_k|}\right] f &= -\sum_{j>k}^{N}\left(\sum_i^N \frac{\partial}{\partial z_i}\frac{1}{|\vec{r}_j - \vec{r}_k|} f - \frac{1}{|\vec{r}_j - \vec{r}_k|}\sum_i^N \frac{\partial}{\partial z_i} f\right) \\ &= -\sum_{j>k}^{N}\left(\left(\frac{\partial}{\partial z_j} + \frac{\partial}{\partial z_k}\right)\frac{f}{|\vec{r}_j - \vec{r}_k|} - \frac{1}{|\vec{r}_j - \vec{r}_k|}\sum_{i=j,k}\frac{\partial}{\partial z_i} f\right) \\ &= -\sum_{j>k}^{N}\left(f\frac{\partial}{\partial z_j}\frac{1}{|\vec{r}_j - \vec{r}_k|} + f\frac{\partial}{\partial z_k}\frac{1}{|\vec{r}_j - \vec{r}_k|}\right) \\ &= -f\sum_{j>k}^{N}\left(-\frac{z_j - z_k}{|\vec{r}_j - \vec{r}_k|^3} + \frac{z_j - z_k}{|\vec{r}_j - \vec{r}_k|^3}\right) \\ &= 0. \end{aligned} \tag{90}$$

Thus the acceleration operator is

$$\hat{a}_z = -Z\sum_{j=1}^{N}\frac{z_j}{r_j^3} + NE(t). \tag{91}$$

B Transition Matrix Elements

Slater-Condon rules [17] are

$$\begin{cases} \langle\phi_0|\,\hat{\mathcal{O}}\,|\phi_0\rangle & = & \sum_{i=1}^{N}\langle\chi_i|\,\hat{o}\,|\chi_i\rangle\,, \\ \langle\phi_0|\,\hat{\mathcal{O}}\,|\phi_a^p\rangle & = & \langle\chi_a|\,\hat{o}\,|\chi_p\rangle\,, \\ \langle\phi_0|\,\hat{\mathcal{O}}\,|\phi_{ab}^{pq}\rangle & = & 0. \end{cases} \tag{92}$$

The expectation value of a general operator for two singly excited wave functions is solved for the different cases as follows:

$$\begin{aligned} &\langle\phi_a^p|\,\hat{\mathcal{O}}\,|\phi_b^q\rangle = \\ &= \begin{cases} \text{a=b, p=q:} & \sum_i^N\langle\chi_i|\,\hat{o}\,|\chi_i\rangle - \langle\chi_a|\,\hat{o}\,|\chi_a\rangle + \langle\chi_p|\,\hat{o}\,|\chi_p\rangle = 0, \\ \text{a=b:} & \langle\phi_a^p|\,\hat{\mathcal{O}}\,|\phi_a^q\rangle = \langle\psi|\,\hat{\mathcal{O}}\,|\psi_p^q\rangle = \langle\chi_p|\,\hat{o}\,|\chi_q\rangle\,, \\ \text{p=q:} & \langle\phi_a^p|\,\hat{\mathcal{O}}\,|\phi_b^p\rangle = -\langle\psi|\,\hat{\mathcal{O}}\,|\psi_b^a\rangle = -\langle\chi_b|\,\hat{o}\,|\chi_a\rangle\,, \\ \text{a}\neq\text{b, p}\neq\text{q:} & \langle\phi_a^p|\,\hat{\mathcal{O}}\,|\phi_b^q\rangle = 0. \end{cases} \end{aligned} \tag{93}$$

In the first case the first Slater-Condon rule has been utilised leading to summation over all spin orbitals in the singly excited Slater determinant, these transition matrix elements are zero as a consequence of the selection rules which prevent interaction between states with the same l value. In the second and third cases the states are one excitation removed from each other. The states are rewritten as a reference state $|\psi\rangle$ and a state one excitation removed from it $|\psi_p^q\rangle$ and $|\psi_b^a\rangle$. The second Slater-Condon rule is then used. In the third case the determinant property that if a column is exchanged with another column the determinant changes sign is utilised. In the fourth case the third Slater-Condon rule is used as the two states are two excitations removed.

The matrix elements in Eq. (58) are calculated as follows:

$$\begin{aligned} \langle\phi_0|\,\hat{H}(t)\,|\phi_0\rangle &= \langle\phi_0|\,\hat{H} - E_0 + \hat{V}(t)\,|\phi_0\rangle = E_0\,\langle\phi_0|\phi_0\rangle - E_0\,\langle\phi_0|\phi_0\rangle - 0 = 0, \\ \langle\phi_0|\,\hat{H}(t)\,|\phi_a^p\rangle &= \langle\phi_0|\,\hat{H}\,|\phi_a^p\rangle - E_0\,\langle\phi_0|\phi_a^p\rangle + \langle\phi_0|\,\hat{V}(t)\,|\phi_a^p\rangle \\ &= 0 + 0 + \langle\chi_a|\,\hat{v}(t)\,|\chi_p\rangle \\ &= \langle\chi_a|\,\hat{v}(t)\,|\chi_p\rangle\,, \\ \langle\phi_a^p|\,\hat{H}(t)\,|\phi_0\rangle &= \langle\chi_p|\,\hat{v}(t)\,|\chi_a\rangle\,, \\ \langle\phi_a^p|\,\hat{H}(t)\,|\phi_b^q\rangle &= \langle\phi_a^p|\,\hat{H} - E_0\,|\phi_b^q\rangle + \langle\phi_a^p|\,\hat{V}(t)\,|\phi_b^q\rangle\,, \end{aligned} \tag{94}$$

where the the Slater-Condon rules, the selection rule, $\Delta l = \pm 1$, of the interaction operator and Brillouins theorem [17], $\langle\phi_0|\,\hat{H}\,|\phi_a^p\rangle = 0$, have been utilised. The first term of the last equation in Eq. (94) solved through utilising the following relation

$$\langle\phi_a^p|\,\hat{H} - E_0\,|\phi_b^q\rangle = (\epsilon_p - \epsilon_a)\delta_{ab}\delta_{pq} + 2\,\langle\chi_p\chi_a|\chi_b\chi_q\rangle - \langle\chi_p\chi_q|\chi_b\chi_a\rangle\,, \tag{95}$$

defined in [17]. The second term is solved using the relation in Eq. (93).

C Numerical Representations of the Transition Matrix Elements

In the numerical method used, the spin orbitals in Eq. (63) are represented as products of a radial function and the spherical harmonics,

$$\chi(r,\theta,\varphi) = R_{nl}(r)Y_l^m(\theta,\varphi). \tag{96}$$

Thus, the transition matrix elements are given by the general formula

$$\langle\chi|\,\hat{o}\,|\chi'\rangle = \langle nl|\,f(r)\,|n'l'\rangle\,\langle lm|\,g(\theta,\varphi)\,|l'm'\rangle\,, \tag{97}$$

where $f(r)$ and $g(\theta,\varphi)$ are the general functions depending on the radial and angular coordinates respectively that make up the general operator $\hat{o}$. The radial integral,

$$\langle nl|\,\hat{f}(r)\,|n'l'\rangle = \int_0^\infty r^2 R_{nl}^* f(r) R_{n'l'} dr = \sum_{\alpha=\beta=1}^{n_s} c_\alpha^{nl} c_\beta^{n'l'} \int_0^\infty B_\alpha^{k_s}(r) f(r) B_\beta^{k_s}(r) dr, \tag{98}$$

is evaluated numerically with a basis set of B-splines $\{B_\alpha^{k_s}(r)\}_{\alpha=1}^{n_s}$, where k_s is the order of the B-spline and n_s the dimension of the basis. The B-splines are real-valued piecewise-polynomial functions with compact support. The B-splines are a commonly used basis for numerical simulations of atomic and molecular systems due to the flexibility of the method, allowing for a continuous function with continuous first and second derivatives between the points. B-splines can provide a more accurate representation of the continuum state than other basis sets and are well suited for the computation of dynamical properties [30].

The angular integrals are solved analytically using the Wigner-Eckart theorem [25]. The initial condition of the wave function can be defined to be the ground state, an excited state or a superposition of states in the atom being investigated.

In order to avoid unphysical reflections, generated when the wave function reaches the end of the simulated box, the exterior complex scaling (ECS) method can be used, it is a way of absorbing the wave function as it reaches the end of the simulation box by adding an exterior region in which space is rotated by some angle θ_{ECS} into the complex plane, for a detailed description, *see* [22]. The basis is separated into three parts, the inner region with n_{inner} points, the linear region with n_{linear} points each with the spacing dR_{linear} and the ECS region with n_{ECS} points with the complex scaling angle θ_{ECS}. The use of the ECS method makes the Hamiltonian non-hermitian, and therefore the norm of the wave function is not preserved. A non-hermitian Hamiltonian has complex eigenvalues, however as the observables must be real one evaluates the transition matrix elements on the inner and linear regions which are unaffected by the ECS [24].

References

[1] H. Hartridge and F. J. W. Roughton. *A method of measuring the velocity of very rapid chemical reactions*. *PROCEEDINGS OF THE ROYAL SOCIETY A*, 104:376–394, 1923.

[2] M. Eigen. *Methods for investigation of ionic reactions in aqueous solutions with half-times as short as 10–9 sec. Application to neutralization and hydrolysis reactions*. *DISCUSSIONS OF THE FARADAY SOCIETY*, 17:194–205, 1954.

[3] T. H. Maiman. *Stimulated Optical Radiation in Ruby*. *NATURE*, 187:493–494, 1960.

[4] M. Chergui and J. M. Thomas. *From structure to structural dynamics: Ahmed Zewail's legacy*. *STRUCTURAL DYNAMICS-US*, 4:043802, 2017.

[5] A. Scrinzi. *Attosecond Physics - Theory*. CreateSpace Independent Publishing Platform, 2014.

[6] E. Goulielmakis, Z. Loh, A. Wirth, R. Santra, N. Rohringer, V. S. Yakovlev, S. Zherebtsov, T. Pfeifer, A. M. Azzeer, M. F. Kling, S. R. Leone, and F. Krausz. *Real-time observation of valence electron motion*. *NATURE*, 466:739–743, 2010.

[7] M. Wu, S. Chen, S. Camp, K. J. Schafer, and M. B. Gaarde. *Theory of strong-field attosecond transient absorption*. *JOURNAL OF PHYSICS B-ATOMIC MOLECULAR AND OPTICAL PHYSICS*, 49:062003, 2016.

[8] A. R. Beck, D. M. Neumark, and S. R. Leone. *Probing ultrafast dynamics with attosecond transient absorption*. *CHEMICAL PHYSICS LETTERS*, 624:119–130, 2015.

[9] R. H. Dicke. *Coherence in Spontaneous Radiation Processes*. *PHYSICAL REVIEW*, 93:99–110, 1954.

[10] M. Gross and S. Haroche. *Super-radiance - an essay on the theory of collective spontaneous emission*. *PHYSICS REPORTS-REVIEW SECTION OF PHYSICS LETTERS*, 93:301–396, 1982.

[11] T. Förster. *Experimentelle und theoretische Untersuchung des zwischenmolekularen Übergangs von Elektronenanregungsenergie*. *ZEITSCHRIFT FÜR NATURFORSCHUNG A*, 4:321–327, 1949.

[12] T. Gallagher and P. Pillet. *Dipole–Dipole Interactions of Rydberg Atoms*. *ADVANCES IN ATOMIC MOLECULAR AND OPTICAL PHYSICS*, 56:161–218, 2008.

[13] D. L. Andrews. *A unified theory of radiative and radiationless molecular energy transfer*. *CHEMICAL PHYSICS*, 135:195–201, 1989.

[14] L. Greenman, P. J. Ho, S. Pabst, E. Kamarchik, D. A. Mazziotti, and R. Santra. *Implementation of the time-dependent configuration-interaction singles method for atomic strong-field processes*. *PHYSICAL REVIEW A*, 82:023406, 2010.

[15] J. J. Sakurai and J. Napolitano. *Modern quantum mechanics*. Addison-Wesley, 2nd edition, 2011.

[16] C. J. Foot. *Atomic physics*. Oxford University Press, USA, 2005.

[17] A. Szabo and N. S. Ostlund. *Modern Quantum Chemistry: Introduction to Advanced Electronic Structure Theory*. Dover Publications, Inc., first edition, 1996.

[18] J. M. Dahlström, S. Pabst, and E. Lindroth. *Attosecond transient absorption of a bound wave packet coupled to a smooth continuum*. *JOURNAL OF OPTICS*, 19:124002, 2017.

[19] J. D. Jackson. *Classical electrodynamics*. Wiley, 3rd edition, 1999.

[20] S. Ravets, H. Labuhn, D. Barredo, L. Beguin, T. Lahaye, and A. Browaeys. *Coherent dipole-dipole coupling between two single Rydberg atoms at an electrically-tuned Forster resonance*. *NATURE PHYSICS*, 10:914–917, 2014.

[21] C. Leforestier, R. H. Bisseling, C. Cerjan, M. D. Feit, R. Friesner, A. Guldberg, A. Hammerich, G. Jolicard, W. Karrlein, H. D. Meyer, N. Lipkin, O. Roncero, and R. Kosloff. *A comparison of different propagation schemes for the time-dependent Schrodinger-equation*. *JOURNAL OF COMPUTATIONAL PHYSICS*, 94:59–80, 1991.

[22] B. Simon. *The definition of molecular resonance curves by the method of exterior complex scaling*. *PHYSICS LETTERS A*, 71:211–214, 1979.

[23] N. Rohringer, A. Gordon, and R. Santra. *Configuration-interaction-based time-dependent orbital approach for ab initio treatment of electronic dynamics in a strong optical laser field*. *PHYSICAL REVIEW A*, 74:043420, 2006.

[24] F. Zapata, J. Vinbladh, E. Lindroth, and J. M. Dahlström. *Implementation and validation of the relativistic transient absorption theory within the dipole approximation*. *ELECTRONIC STRUCTURE*, 3:014002, 2020.

[25] I. Lindgren and J. Morrison. *Atomic Many-Body Theory*. Springer-Verlag Berlin Heidelberg, 2nd edition, 1986.

[26] D. Chandler. *Introduction to Modern Statistical Mechanics*. Oxford University Press, 1987.

[27] P. Eng-Johnsson. personal communication, March 29, 2021.

[28] H. A. Bethe and E. E. Salpeter. *Quantum Mechanics of One- and Two-Electron Atoms*. Springer, Berlin, Heidelberg, 1957.

[29] A. Kono and S. Hattori. *Accurate oscillator strengths for neutral helium*. *PHYSICAL REVIEW A*, 29:2981–2988, 1984.

[30] H. Bachau, E. Cormier, P. Decleva, J. E. Hansen, and F. Martin. *Applications of B-splines in atomic and molecular physics*. *REPORTS ON PROGRESS IN PHYSICS*, 64:1815–1943, 2001.